

**Experimental study of the liquid velocity and turbulence in a large-scale air-water counter-current bubble column**

Ziegenhein, T.; Besagni, G.; Inzoli, F.; Lucas, D.;

Originally published:

October 2019

**Experimental Thermal and Fluid Science 111(2020), 109955**

DOI: <https://doi.org/10.1016/j.expthermflusci.2019.109955>

Perma-Link to Publication Repository of HZDR:

<https://www.hzdr.de/publications/Publ-26513>

Release of the secondary publication  
on the basis of the German Copyright Law § 38 Section 4.

CC BY-NC-ND

# Experimental study of the liquid velocity and turbulence in a large-scale air-water counter-current bubble column

Thomas Ziegenhein<sup>1,3</sup> \*, Dirk Lucas<sup>1</sup>, Giorgio Besagni<sup>2</sup>, Fabio Inzoli<sup>2</sup>

<sup>1</sup> Helmholtz-Zentrum Dresden-Rossendorf e.V., 01314 Dresden, Germany

<sup>2</sup> Politecnico di Milano, Department of Energy, Via Lambruschini 4a, 20156 Milano, Italy

<sup>3</sup> School for Engineering of Matter, Transport and Energy, Arizona State University, Tempe, AZ 85287, USA

\* Corresponding author. Tel.: +49 3512602503; fax: +49 3512603440.

E-mail address: t.ziegenhein@hzdr.de (Thomas Ziegenhein).

## Abstract

Measuring the local liquid velocity and turbulence in large-scale bubble columns with optical methods is complex and usually limited to low gas holdups in thin geometries. Comprehensive datasets in large bubble columns are therefore seldom published. Since the importance of Computational Fluid Dynamics (*CFD*) is increasing for multiphase applications, such data is also important for validating models for dispersed bubbly flows. In the present work the liquid velocity and turbulence in a pilot-scale bubble column is studied and a *CFD* validation database is generated by completing previous measurements of the gas void fractions and bubble sizes. For this purpose, we used a Particle Shadowgraph Velocimetry (*PSV*) technique that was intentionally designed to study the fluid dynamics in large-scale facilities. The measurements were realized in the 5.3 m high and 0.24 m diameter counter-current bubble column at Politecnico di Milano. The superficial gas velocity ranged from 0.37 to 1.85 cm/s, the counter current superficial liquid velocity from 0 to 9.2 cm/s. All operation points are in the so-called pseudo-homogeneous flow regime, in which the integral gas holdup (ranging from 1.02 to 7.55 %) increases linear with the superficial gas velocity but an inhomogeneous flow is present. The dominant frequencies of the bubbly flow, shear rates, and turbulence levels are increasing with increasing superficial gas velocity. With increasing superficial liquid velocities, the dominant frequencies are decreasing, the averaged liquid velocities are shifted downwards, but the overall turbulence levels remain constant. In order to investigate the smaller scales at which the bubble-induced turbulence is expected, a filtering process is proposed. As a result, the filtered turbulence levels of all operation points fall on a linear trend line when plotted over the local void fraction, which is the same result obtained in other studies in small, homogenous tabletop columns. The now available database for *CFD* validation contains the averaged liquid velocities, basic turbulence information, local void fractions, and the bubble sizes at two different heights. The data will be in particular useful to

validate the capabilities of models to upscale bubbly flows from tabletop to the pilot-scale bubble columns.

**Keywords**

Bubbly flows, particle-tracking velocimetry, multiphase turbulence, pilot-scale bubble columns, CFD database

# 1 Introduction

Bubbly flows are characterized by the strong connection of three main parameters: (a) liquid velocity, (b) gas fraction, and (c) bubble size distribution. Specifically, the fluid dynamics in bubble columns are subject to this connection since the bubbles drive the liquid flow, which in reverse influence the rising characteristic and break-up/coalescence of the bubbles. In particular, the local-scales (i.e. break-up/coalescence, force balance, etc.) are strongly coupled to the integral-scale (i.e. gas-holdup, flow regime, etc.). Consequently, all three parameters need to be considered in order to understand the dynamics of bubbly flows and to improve the modeling strategies at the different scales.

Usually for the three parameters mentioned above, different measuring techniques are used. With probes, the local gas volume fraction is relatively simple accessible (Schleicher et al. 2008). Measuring the Bubble Size Distribution (*BSD*), however, is more complicated. Nevertheless, evaluating bubble sizes manually from pictures is a simple but time-consuming method with which reasonable results can be obtained in optical assessable setups (e.g. Besagni & Inzoli (2016a)). The methods for measuring the liquid velocity in bubbly flows are manifold and adapted from single-phase flows. The most frequently used methods are Particle Image Velocimetry (*PIV*) (e.g. (Hessenkemper & Ziegenhein 2018)), Laser Doppler Anemometry (*LDA*) (e.g. (Hosokawa & Tomiyama 2013)), and Hot Film Anemometry (*HFA*) (e.g. (Rensen et al. 2005)). In the large group of *PIV* methods with (Deen et al. 2002) and without (Ziegenhein et al. 2016a) laser illumination falls the Particle Tracking Velocimetry (*PTV*) method, which is used in the present work. When no lasers are used for *PIV* measurements, usually a background light is applied so that the shadows of particles are recorded, which is called Particle Shadowgraph Velocimetry (*PSV*) (Hessenkemper & Ziegenhein 2018). *PSV* methods are not common, but they have some advantages in bubbly flows.

One advantage of *PSV* methods is the possibility of a permanent light source so that no extra trigger is needed, which simplifies the setup distinctly. However, more importantly for a field measurement is that background lights has very little safety requirements compared to a laser. This advantage is often vital to perform measurements at large test facilities built up in a non-laser lab environment. From our experience, another advantage of background light is that they can be used at higher volume fractions in bubbly flows. A two-dimensional laser light sheet is distorted at the bubble surface so that on one hand, large shadows behind the bubbles occur and on the other hand, particles are illuminated before and behind the supposed two-dimensional measurement plane due to reflections. A technical advantage is that no fluorescence tracers are needed. Particles with a fluorescent pigment coated on the particle surface contaminate the bubbly flow distinctly since the pigment is usually hydrophobic. Particles with an encapsulated pigment are expensive (considering a fluid volume of around 200 liter), often limited to specific sizes or are not neutrally buoyant. However, the disadvantage of background light is the volume illumination and the connected problem of selecting particles on a two-dimensional plane.

41 This is realized in the present work by using a thin depth of field and selecting sharp  
42 particles in the post-processing.

43 By using *PTV* instead of *PIV*, further problems are avoided. First, masking bubbles  
44 (Jakobsen et al. 1996) (Pang & Wei 2013) in the post processing or even recording the  
45 bubbles in a separate step (Delnoij et al. 2000) (Bröder & Sommerfeld 2007) is not  
46 necessary. A second advantage of *PTV* is that a lower tracer-particle density can be used.  
47 Because the velocity is measured in gaps of rising bubble swarms in the present study, a  
48 relatively high spatial resolution – i.e. small interrogation areas – for *PIV* would be needed.  
49 Such a high spatial resolution requires a high seeding, which blocks the light and causes a  
50 distinct contamination of the bubbles with tracers. Another problem with *PIV* in dense  
51 bubbly flows is that neighboring interrogation areas are masked due to the presence of the  
52 bubbles. Since robust single-phase flow *PIV* algorithms use neighboring interrogation areas  
53 for iteration or validation, those would be not applicable. With the chosen particle seeding  
54 and spatial resolution, *PTV* can handle higher void fractions. Nevertheless, *PIV* methods  
55 work well in bubble free zones (Murgan et al. 2017), discrete gas sparger setups (Lindken  
56 & Merzkirch 2002) (Rzehak et al. 2017) or low void fractions (Delnoij et al. 1999). Using  
57 techniques that are more advanced, like the *LIF-PLV* technique described by Bröder and  
58 Sommerfeld (2002), dense bubbly flows can be investigated with *PIV*. Certainly, all *PTV* and  
59 *PIV* techniques are behind one-point measurements like *LDA* (Mudde et al. 2009) and *HFA*  
60 (Mercado et al. 2012) in terms of maximum void fraction. However, these measuring  
61 techniques have also some drawback and the phase discrimination is not trivial.

62 Due to the described advantages, *PTV* combined with a shadowgraph setup, called from  
63 here on Particle Shadowgraph Tracking Velocimetry (*PSTV*), was used in the present study.  
64 The measurements were conducted at the counter-current bubble column located at the  
65 Department of Energy of Politecnico di Milano (Besagni & Inzoli 2016a) (Besagni et al.  
66 2017). The 5.3 m high and 0.24 m diameter column was developed concerning the well-  
67 known scaling-up criteria “*large-diameter*” and the “*large-scale*” concepts, discussed in the  
68 pioneering study of (Wilkinson et al. 1992) and, more recently by (Besagni et al. 2017a),  
69 where the “*large-diameter*” concept has been related to the Rayleigh–Taylor instabilities  
70 (Kitscha, & Kocamustafaogullarim, 1989). The gas was distributed in the column at the  
71 bottom via a spider-sparger that is typically used in industrial applications. The dimensions  
72 of the bubble column are therefore in the range of a pilot-scale facility that is used to scale-  
73 up results from laboratory-scale to the final, industrial scale (Shaikh & Al-Dahhan, 2013). In  
74 addition, the facility is equipped with a water pump so that the liquid can be recirculated in  
75 an external loop. Gas superficial velocities were used in the range of  $U_G = 0.37\text{--}1.85$  cm/s,  
76 the liquid was recirculated at several superficial liquid velocity from  $U_L = 0.0$  cm to  $9.2$   
77 cm/s, where  $0.0$  cm/s refers to the batch mode (i.e. gas is dispersed in a standing liquid  
78 column). All experiments were performed in the boundaries of the pseudo-homogeneous  
79 flow regime, as classified by Besagni et al. (2016a, b) (2018). The gas holdup, in the above-  
80 mentioned conditions, was ranging from 1.02 to 7.55 %.

81 From the measurements, the transient as well as time-averaged liquid velocities are  
82 determined. The components of the Reynolds stress tensor are distinctly influenced by a  
83 bubble plume found in the column. Therefore, a filtering process is proposed with which  
84 the smaller-scales can be investigated. Comparing the filtered results to other  
85 measurements in small-scale bubble columns, surprising similarities are found, which  
86 indicate a similarity of the bubble induced turbulence. Bubble induced turbulence in  
87 general is an important effect in order to model for example coalescence and break-up  
88 (Liao & Lucas 2009) or mixing (Almérás et al. 2015) correctly. In the recent years, the  
89 turbulence in bubbly flows is subject to many publications, from single bubble  
90 investigations (Liu et al. 2005) over bubble columns (Julia et al. 2007) to two-phase pipe  
91 flows (Hosokawa & Tomiyama 2013). With increasing computational power, the topic is  
92 also in the focus of Direct Numerical Simulations (*DNS*) (Ma et al. 2017) and Large Eddy  
93 Simulations (*LES*) (Fraga et al. 2016). Several models exist with specific aims, for example  
94 the (Reynolds Averaged Navier Stokes) RANS modeling is reviewed by Rzehak & Krepper  
95 (2013a) and a model to match the often reported slope deviation in the energy spectra is  
96 proposed by Riboux et al. (2013). In the present work, we evaluate the change of the  
97 bubble induced turbulent kinetic energy with the (local) void fraction with a filtering  
98 process. Further, the findings are compared to the experiments of Julia et al. (2007) as well  
99 as Lance & Bataille (1991) and to the linear hypothesis of Nigmatulin (1979).

100 Such velocity measurements at pilot-plant scale are rarely reported in the literature, in  
101 particular for counter-current bubble columns. The present measurements complete  
102 previous gas volume fraction and bubble size measurements (Besagni & Inzoli 2016a) to  
103 provide a comprehensive *CFD* validation database. Such data that covers the continuous  
104 and dispersed phase properties resolved locally at different position in the facility are vital  
105 for advancing the model development (Lucas et al. 2016).

## 106 2 Experimental setup and methods

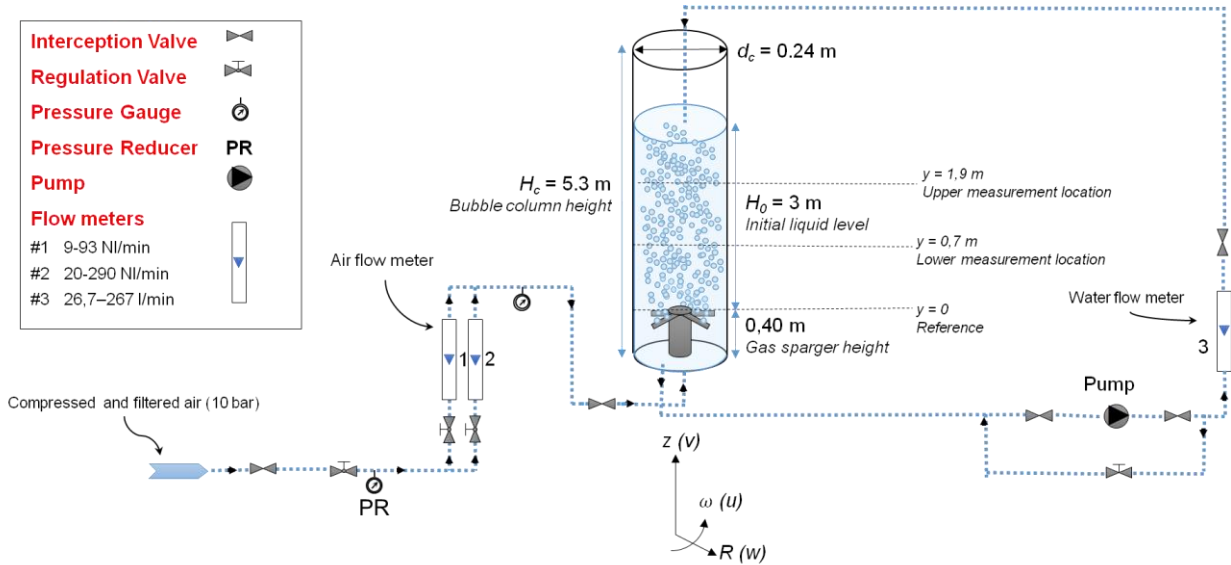
107 This section aims to present the experimental setup and to provide the needed background  
108 to better interpret the experimental data. First, the experimental setup is briefly described;  
109 second, the *PTV* method is introduced. The reader may refer to Appendix A for a discussion  
110 concerning the prevailing flow regimes, the local and the global flow properties in the  
111 conditions examined in this paper are briefly discussed. In addition, a discussion of the flow  
112 regimes in large-scale bubble columns can be found in our recent review paper (Besagni et  
113 al. 2018).

### 114 2.1 Experimental setup

115 The experimental facility (Figure 1) is a non-pressurized vertical pipe made of Plexiglas. A  
116 pressure reducer controls the pressure upstream of the rotameters (1) and (2), which are  
117 used to measure the gas flowrate (E5-2600/h, manufactured by ASA, Italy). The accuracy of  
118 the measured integral gas flow rate is  $\pm 2\%$  with a repeatability error of under  $\pm 0.25\%$ . A

119 pump, which is controlled by a bypass valve, provides water recirculation and a rotameter  
 120 (3) measures the liquid flowrate (G6-3100/39, manufactured by ASA, Italy). The accuracy  
 121 of the measured liquid flow rate is  $\pm 1.5\%$  with a repeatability error of under  $\pm 0.5\%$ . The  
 122 air distributor is a spider-gas sparger, which is similar to the distributors used in industrial  
 123 application. The spider sparger, shown in Figure 2, has six arms (120 mm diameter, made  
 124 of stainless steel) tubes soldered to the central cylinder of the sparger. The angle between  
 125 the different tubes is  $60^\circ$ . There are six holes (hole-diameters in the range of 2–4 mm,  
 126 Figure 2c and Figure 2d) located on the side of each arm facing upward; these holes are  
 127 distributed as shown in Figure 2d, with the hole diameter increasing toward the column  
 128 wall. In addition, there are four holes, located on the header of the gas sparger, located as is  
 129 Figure 2d. A porous plate has been included in the lower part of the gas sparger, to ensure a  
 130 uniform liquid velocity profile and avoid preferential path induced by the water outlet.  
 131 Owing to the gas sparger opening, the produced bubble size distribution (*BSD*) is  
 132 polydispersed (Figure 29, in Appendix A). Filtered air and filtered, deionized water were  
 133 used; during the experiments, the air and water temperatures were maintained constant at  
 134 room temperature ( $22^\circ\text{C}$ ). The values of the gas density, which were used to compute the  
 135 superficial gas velocity,  $U_G$ , are based upon the operating conditions existing at the column  
 136 midpoint (Reily et al. 1994) and are computed by using the ideal gas law.

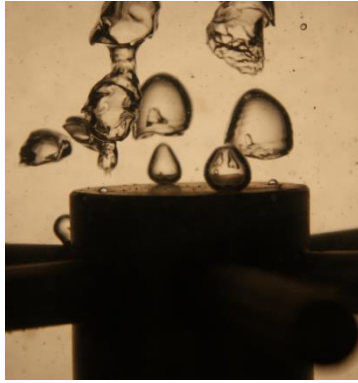
137



138

139

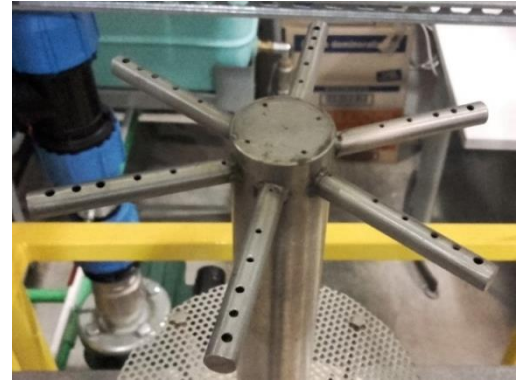
Figure 1 The experimental setup



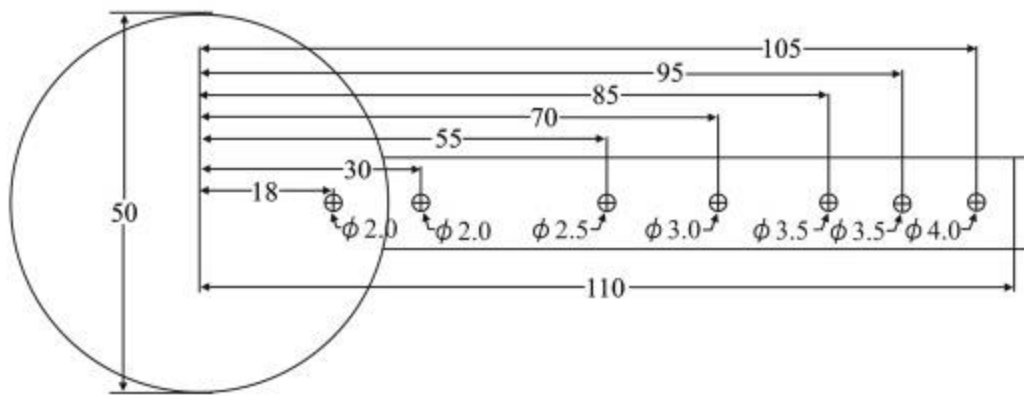
(a) Bubbles at the gas sparger at low sup. gas velocity



(b) Spider gas sparger



(c) View from top

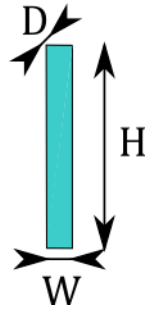
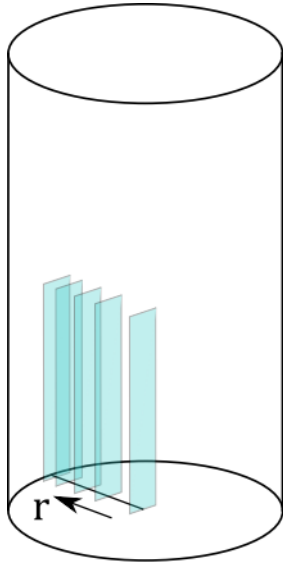


(d) Spider gas sparger: distribution and diameter of the holes on one of the arms (measurements in mm)

140 Figure 2 The gas sparger (spider-sparger) – Besagni et al. (2017) and Besagni and Inzoli,  
 141 (2016a)

## 142 2.2 Measurement setup

143 The liquid velocity measurements were realized at the two measuring heights where the  
 144 previous optical probes measurements took place (see Besagni and Inzoli (2016a)), namely  
 145 at  $h= 1.9$  m and 0.7 m above the gas-sparger. As explained in the introduction, the  
 146 measuring concept is a shadowgraph technique with a backlight, which was an air-cooled  
 147 400W halogen lamp. To obtain a quasi-two-dimensional measuring plane, the depth of field  
 148 was adjusted to 2 mm by using a Samyang lens with an aperture of 2.0, a focal length of  
 149 135, and a focus distance of 1300 mm. The optical setup with the Q-VIT high-speed camera  
 150 from AOS Technologies AG was placed on a linear unit ( $\pm 0.020$  mm on 300 mm) to move it  
 151 stepwise along the column radius. With this method, we obtained 11 measuring planes of  
 152 6x25.3 mm (Width x Height) with a resolution of 397x1686 pixels along the radial  
 153 coordinate as shown in Figure 3. The positions of the planes were chosen so that near the  
 154 wall, where higher gradients of the time averaged liquid velocities are expected, a higher  
 155 radial resolution is obtained.



W = 6 mm, H = 25.3 mm, D = 2 mm,  
 Resolution = 0.0115 mm/Pixel,  
 Measuring time per plane = 1000 s

Position	Radial coordinate, r [m]
1	0.119
2	0.116
3	0.113
4	0.110
5	0.100
6	0.090
7	0.080
8	0.060
9	0.040
10	0.020
11	0.000

156 Figure 3 Scheme of the measuring concept.

157 In order to minimize optical distortions due to the round shape of the bubble column, a box  
 158 filled with water was placed around the bubble column. Since the water in the box and the  
 159 Plexiglas® of the bubble column have almost the same refraction index, it is assumed that  
 160 no optical distortion due to round shape of the bubble column is present. This concept has  
 161 been verified in a previous study by Besagni and Inzoli (2016b), in an annular gap bubble  
 162 column, to whom the reader may refer. In addition, this is a common technique for PIV  
 163 measurements in round shapes, e.g. in pipes (van Doorne & Westerweel 2007). The linear  
 164 unit was moved perpendicular to the box, the radial positions in the bubble column were  
 165 calculated with the refraction index of water. The measurements were calibrated by using a  
 166 microscope calibration plate with an accuracy of  $10^{-4}$  mm. In the following, the horizontal  
 167 velocity in the planes is referred as angular velocity. Due to the narrow measuring plane of  
 168 6 mm, the off-set error to an circle for the measuring position at a radial coordinate of 0.02  
 169 m would be 0.500 mm. Therefore, this geometrical error is neglected in the following.

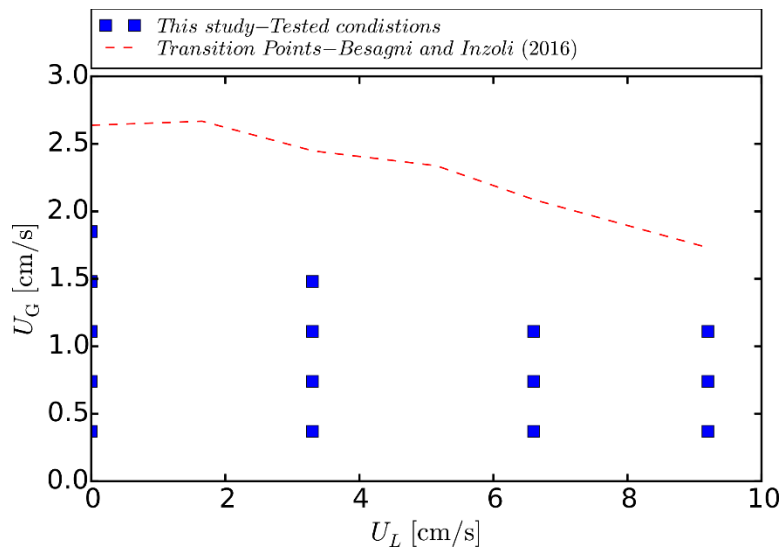
170 This method of moving the camera in radial direction at the two heights is executed for the  
 171 15 flow-configuration listed in Table 1 so that in total 330 single experiments were  
 172 conducted. The tested conditions are plotted against the determined regime transition  
 173 points in Figure 4: all experiments are situated below the transition point in the pseudo-  
 174 homogenous regime. In fact, the flow configurations were determined by the optical  
 175 accessibility of the flow field from the outside. As will be discussed in the following sections,  
 176 above 6 or 8 % integral gas holdup, depending on the bubble size, meaningful  
 177 measurements with the present technique were not possible in this large-diameter column.

178 Table 1 Operating conditions evaluated in the present study (marked as ✓); in brackets is  
 179 the integral gas holdup at this operation point given (Besagni and Inzoli, 2016a).  
 180 Accordingly with the uncertainty analysis on the gas holdup measurements proposed in

181 (Besagni et al. 2017), the gas holdup are measured with an absolute error estimated below  
 182  $\pm 0.02$  %.

Sup. gas velocity [cm/s] → Sup. liquid velocity [cm/s] ↓	0.37	0.74	1.11	1.48	1.85
0.0 (batch mode)	✓ (1.02 %)	✓ (1.64 %)	✓ (3.72 %)	✓ (5.30 %)	✓ (6.60 %)
-3.3 (counter-current mode)	✓ (1.32 %)	✓ (2.91 %)	✓ (4.61 %)	✓ (6.63 %)	
-6.6 (counter-current mode)	✓ (1.70 %)	✓ (3.62 %)	✓ (5.99 %)		
-9.2 (counter-current mode)	✓ (2.44 %)	✓ (5.00 %)	✓ (7.55 %)		

183



184

185 Figure 4 Operating conditions evaluated in the present study (blue) compared with the  
 186 regime transition point (red line) determined by Besagni & Inzoli (2016a).

187 With tracer particles glued between glass plates, the 2 mm depth of field of the camera  
 188 setup was calibrated as described in our previous work (Ziegenhein et al. 2016a). The  
 189 aperture of the lens and the thresholds of the post processing algorithms were adjusted to  
 190 a depth of field of around 2 mm. It should be noted that the illumination of the particles in  
 191 the flow is not the same as in the calibration so that the 2 mm are only a reference value.  
 192 However, the used setup is very large compared to the depth of field so that even  $\pm 1$  mm  
 193 uncertainty is negligible on the 120 mm long radial coordinate. The flow was seeded with 2  
 194 g of 50  $\mu\text{m}$  Polyamide 12 particles from DANTEC DYNAMICS A/S with a density of 1010  
 195  $\text{kg}/\text{m}^3$ . A set of 10 images with 1000 frames per second was recorded every 2 seconds for  
 196 1000 seconds for all 11 measuring planes so that in total 55 000 images in 3 hours  
 197 measuring time were recorded per operation point. This procedure was equal for all 15  
 198 operating conditions at both measuring heights resulting in 1.65 million images.

199 In the following sections, mainly two averages will be used. For the transient results, the  
 200 average over the measuring plane and over the burst of 10 images (9 sets of images from  
 201 which the particles can be tracked) is used, i.e.

$$\langle v \rangle (T_i, R_j) = \frac{1}{9} \int_{T_i + \frac{1}{100}s}^{T_i} \int_{R_j} v(x, t)_{R_j} dA dt, \quad (1)$$

202 With  $\langle v \rangle (T_i, R_j)$  the averaged velocity over the measuring plane  $dA$  at time  $T_i$  and radial  
 203 coordinate  $R_j$ . The average is calculated over all 10 images recorded in one burst, which is  
 204 equal to a time of 1/100 s. This average is available every two seconds over the 1000  
 205 seconds long measuring period. Every measuring plane  $P_j$  has a radial coordinate  $R_j$  so that  
 206 this average is also a function of the position. For the steady state results, the time-  
 207 averaged value over the entire measuring time,  $\bar{v}(R_j)$  at the radial coordinate  $R_j$  is used, i.e.

$$\bar{v}(R_j) = \frac{1}{T} \int_{1000s}^{0s} \omega \langle v \rangle dt \quad (2)$$

208  
 209 , where  $\omega$  represents the hold processor, which is explained in the following sections, and  
 210  $\langle v \rangle$  the velocity calculated from Eq. (1). This average is only a function of the radial  
 211 coordinate and can be used for comparison with simulations. The averaging indicators  $\langle \rangle$   
 212 and  $\bar{\phantom{x}}$  will be omitted where it is clear which average is meant. When not otherwise stated,  
 213 the normal Reynolds stresses are calculated by

$$\overline{v'v'}(R_j) = \frac{1}{T} \int_{1000s}^{0s} \left( \bar{v}(R_j) - v(x, t)_{R_j} \right)^2 dt \quad (3)$$

214  
 215 , where  $v(x, t)_{R_j}$  are the instantaneous velocities measured on plane  $R_j$ .

### 216 2.3 Optical distortion

217 Due to the different refraction indices from air and water, an optical distortion is present.  
 218 As mentioned above, the distortion due to the round geometry is handled with a square box  
 219 around the bubble column. This is a common technique and therefore the error due to this  
 220 is neglected at this point. Moreover, the camera was carefully aligned to the box around the  
 221 column so that it is assumed that the view is perpendicular. Nevertheless, the light beams  
 222 are not hitting the lens perpendicular, which causes a negligible bending of the depth of  
 223 field. This error is discussed in Appendix C.

## 224 3 Particle Tracking Velocimetry (*PTV*)

225 The used *PTV* method can be separated in two steps, the particle identification and particle  
226 tracking. Both methods are shortly discussed in the following subsections, and a detailed  
227 description can be found in (Hessenkemper & Ziegenhein 2018). A sampling bias is present  
228 in multiphase flows due to the coupling of the dispersed phase with the continuous phase.  
229 The sampling bias will be treated with a hold processor, which is shortly discussed in an  
230 extra subsection. Detailed information about the sampling bias in dispersed multiphase  
231 flows can be found in (Ziegenhein & Lucas 2016b). Finally, we verify the method and the  
232 sampling bias treatment by considering the integral values and comparing the *PSTV*  
233 method to *PIV* methods in a simplified measurement setup.

### 234 3.1 Particle Identification

235 Due to the changing background in multiphase flows (Figure 5 (a)) particle identification is  
236 not trivial. From our experience, methods based on the gradients calculated from the grey  
237 values are applicable. The background has usually small gradients so that a simple  
238 threshold on the Euclidian norm of the gradient vector field is working well. However, due  
239 to an inhomogeneous illumination of particles the contours are often not closed. To close  
240 reliably the contours, a shape recognition algorithm is needed.

241 Shape recognition algorithms are widely used, in particular if simple shapes like circles  
242 need to be identified. A relatively robust class of algorithms is based on the Hough  
243 transform with which the gradients of a picture (Figure 5 (b)) can be transformed in a  
244 parameter space. In contrast to the classic method, the method we use in the present work  
245 is a Hough transform based on the pixels that are not on the particle edges. For speed-up,  
246 we identify potential particles beforehand. The method is designed for a large amount of  
247 small circles rather than identifying a small amount of large circles.

248 However, a main problem of identifying small circles is the representation of such on the  
249 grid of the optical sensor. This representation leads to complex shapes, which are irregular  
250 and asymmetric. This problem can be handled by evaluating the shape on sub pixel  
251 position. Nine points per pixel was a good compromise between accuracy and computation  
252 time for the present purpose (Hessenkemper & Ziegenhein 2018).

253 Looking at the discrete representation of circles on a grid, a circle with a specific radius can  
254 only have edge pixels in a certain distance around his center. Therefore, when the center  
255 (sub-) pixel position is found and the correct radius is known, a specific number of edge  
256 particles should be found on this radius. Using this knowledge, the distance to the edge  
257 pixels for each sub-pixel position in a radius of three pixels is calculated and distributed in  
258 a discrete classification of particle sizes (Table 2). The particle size classification is  
259 obtained from the analytical solution of circles on a mesh. The particle size with the largest  
260 amount of edge pixels is registered to the sub-pixel position. If two particle sizes have the  
261 same amount of edge particles, the larger particle size will be taken. The local maxima of

262 the resulting parameter space are the particle center positions with the assigned particle  
 263 size. To avoid spurious particle identification, the introduction of a minimum edge pixel  
 264 count for each particle size is necessary. If the count is below this value, the edge particle  
 265 count is set to zero.

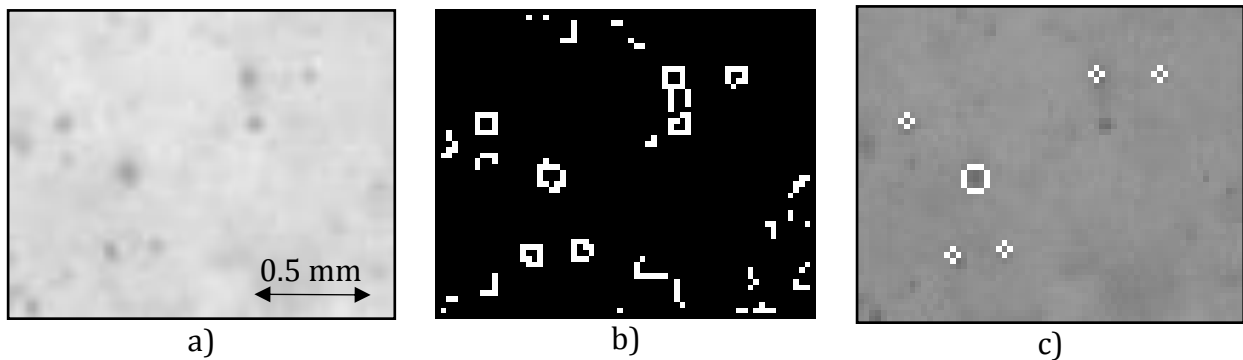
Circle radius [Px]	Set of possible distances [Px <sup>2</sup> ]	Minimal edge pixels
1.0	$1 \leq D^2 \leq 2.25$	6
1.25	$1 \leq D^2 \leq 3.25$	7
1.5	$1.25 \leq D^2 \leq 4.5$	8
1.75	$2 \leq D^2 \leq 5$	9
2.0	$2 \leq D^2 \leq 6.25$	10
2.25	$5 \leq D^2 \leq 8.5$	12
2.5	$5 \leq D^2 \leq 10.25$	14
2.75	$8 \leq D^2 \leq 12.25$	16
3	$8 \leq D^2 \leq 13$	18

266 Table 2 Classification of the circle size depending on the distance, D, to the edge pixels.

267 An example of the particle identification is shown in Figure 5 (c). Figure 5 shows a bubble-  
 268 free, small magnification of the original recorded image (cf. for example Figure 6). The  
 269 large particle identified in Figure 5 (c) is an agglomeration of tracer particles or a  
 270 microbubble naturally occurring in the flow. Particles or particle agglomerations over 75  
 271  $\mu\text{m}$  are not used for tracking, which includes the large particle identified in Figure 5 (c). To  
 272 increase the sub-pixel accuracy, the grey values inside the found circles are fitted to a two-  
 273 dimensional Gaussian function

$$f(x, y) = A \exp \left[ -\frac{(x - x_0)^2}{2\omega_x} - \frac{(y - y_0)^2}{2\omega_y} \right] + \epsilon_{xy} \quad (4)$$

274



275 Figure 5 Magnification of a picture to illustrate the particle identification process. a) Image  
 276 for particle identification, b) the gradient field calculated with the Sobel operator with a  
 277 threshold and c) the identified particles colored white based on the above-discussed  
 278 algorithm (Hessenkemper & Ziegenhein 2018).

## 279 3.2 Particle Tracking

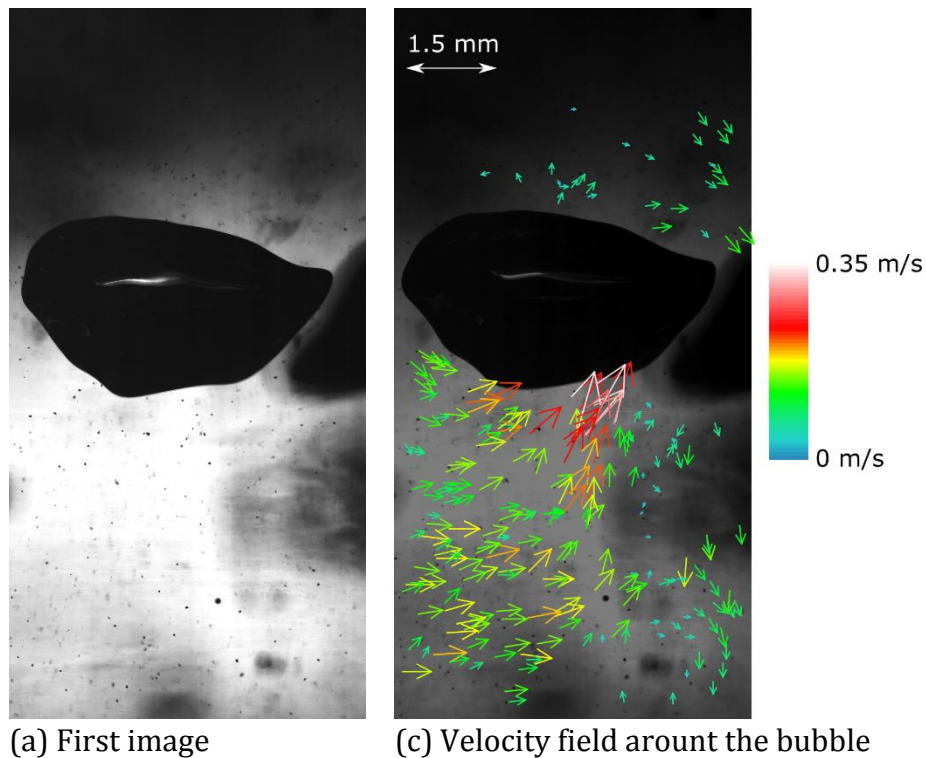
280 For tracking the identified particles, we used a brute force algorithm with a correction step.  
281 The basic idea of the algorithm is to find patterns of tracer particles in the subsequent  
282 image, which is a combination of classic PTV and PIV algorithm. The method is in detail  
283 explained by Hessenkemper & Ziegenhein (2018). A correction step is needed in the  
284 present setup since bubbly flows have usually a strong velocity component perpendicular  
285 to the measuring plane. Therefore, many tracer particles travel outside the observation  
286 area during the measurement. The resulting change of the tracer patterns is causing  
287 spurious vectors, which need to be corrected based on the neighboring particle tracks.

288 The identification of outliers is not trivial; a usual approach that uses the standard  
289 deviation of the entire set of vectors is not useful since they overweight the outliers.  
290 Therefore, a representative set of vectors with which the standard deviation can be  
291 calculated is searched. The representative set is determined around the highest  
292 concentration of velocities transferred to a discretized velocity map. By using a velocity  
293 map, the direction of the velocity is included. The discretization of the velocity map is  
294 circular and overlapping to avoid the drawbacks of a rectangular discretization. Identified  
295 spurious vectors were re-iterated with the particle-tracking algorithm under the side  
296 condition of the averaged velocities found in the cell with the highest velocity count. This  
297 procedure was only applied when the velocity count per set of images was higher than ten  
298 velocities. The allowable maximum velocity was set to 0.85 m/s, the size of the  
299 discretization cells on the velocity map was 0.23 m/s, and 3.5 times of the vector standard  
300 deviation in the cell with the maximum velocity count was allowed. The maximum velocity  
301 allowed was determined from test measurements where spurious vectors were sorted out  
302 by hand and all of the measured velocities were below 0.65 m/s; we added 0.2 m/s to this  
303 value in order to capture rare events of high velocities. The size of the cells on the velocity  
304 map is chosen arbitrary to the rise velocity of the bubbles in still water. Based on a normal  
305 distribution, a standard deviation of 3.5 was chosen so that 99.9% of the velocities are  
306 included. With a spatial resolution of around  $1.5 \cdot 10^{-7}$  m, we reached a nominal resolution  
307 of around 0.0115 m/s per pixel when recording with 1000fps.

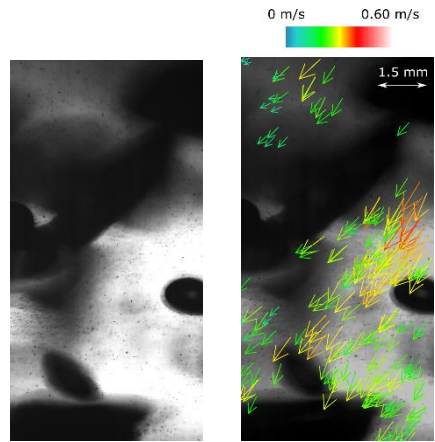
308 The result of the tracking algorithm at a very low gas fraction is shown in Figure 6. The  
309 challenges of tracking the velocities for the present case can be seen nicely from this  
310 example. From the perspective of particle identification, the image has a very  
311 inhomogeneous illumination; while particles in the overexposed areas can be identified  
312 easily with the gradient method, the particle edges are hardly distinguishable from the  
313 darker background in the under exposed areas. Therefore, the noise is very high in these  
314 areas, which would lead to many false particle identifications. However, the particle  
315 identification based on the Hough transform gave robust results in these areas compared to  
316 other techniques like the Canny algorithm (Canny 1986). From the perspective of particle  
317 tracking, the flow field around a bubble is very complex so that high out of plane velocities,  
318 a high range of velocities, high shear fields, and small-scale vorticities occur. As explained  
319 above, the high out of plane velocity is tried to address by tracking patterns of particles and

320 using a re-iteration correction step. The wide range of flow phenomena at a low resolution  
321 is handled by the tracking algorithm well.

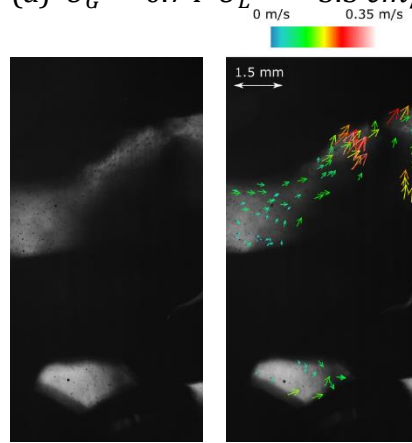
322 While at low gas fractions many particles are visible, the situation is changed at higher gas  
323 fractions (Figure 7). At around 7-percentage gas fraction in the 0.24 m thick reactor only  
324 small areas in which particles can be tracked are occasionally available. Due to the slip  
325 velocity of the bubbles, these areas are closing from one picture to another so that particles  
326 are additionally lost. This is causing more and more spurious vectors, which have to be  
327 identified, re-iterated and sorted out if necessary. Additionally, this might cause a sampling  
328 bias as explained in the following section.



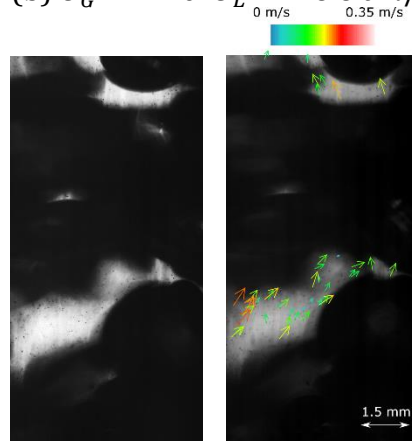
329 Figure 6 Velocity field obtained for a superficial gas velocity of 0.37 cm/s and a superficial  
330 liquid velocity of 0 cm/s (batch mode).  
331



(a)  $U_G = 0.74$   $U_L = -3.3$  cm/s



(b)  $U_G = 1.10$   $U_L = -6.6$  cm/s



(c)  $U_G = 1.85$   $U_L = -0.0$  cm/s

332 Figure 7 Examples of the measured liquid velocity for different superficial gas and liquid  
 333 velocities.

### 335 3.3 Sampling bias

336 Sampling bias exist in multiple ways in multiphase flows. As discussed in our previous  
 337 work (Ziegenhein & Lucas 2016b), a significant bias is present due to the correlation  
 338 between the gas volume fraction and the liquid velocities. This correlation is problematic  
 339 since high gas volume fractions, which are usually connected to high liquid velocity fields,  
 340 block the optical measurements so that less information are measurable in this situation.  
 341 This leads to a correlation between the count of measured particle tracks and the velocity,  
 342 which leads to a sampling bias. In Figure 8 this correlation is shown for the center of the  
 343 column. In Figure 8 are shown the average velocities  $\langle v \rangle$  (cf. Section 2.2) and the track  
 344 count of this averaging procedure at the different measuring times in the center of the  
 345 column. Certainly, more tracks are recorded when the velocity is low and vice versa, which  
 346 causes a negative correlation coefficient of  $-0.288$ . A hold processor as developed in our  
 347 previous work (Ziegenhein & Lucas 2016b) can now be used to correct this bias. Since we  
 348 covered a relatively large measuring area, in almost all recordings some tracked velocities  
 349 are present. Therefore, we do not need to wait in time so that we can simplify the hold  
 350 processor by just averaging the velocity over the measuring area per time step (i.e. the 10  
 351 recorded frames per time step). In order to get the correct, unfiltered Reynolds stresses,  
 352 the turbulence parameters take this averaging into account (Ziegenhein & Lucas 2016b). In  
 353 Figure 9, the time-averaged values  $\bar{v}$  are compared with and without the hold processor.  
 354 Every measuring plane gives one value on the radial coordinate. When we look at the  
 355 velocity profile over the radius (Figure 9), the effect is larger in the center due to the larger  
 356 distance to the camera and therefore a higher gas fraction that can block the camera view.

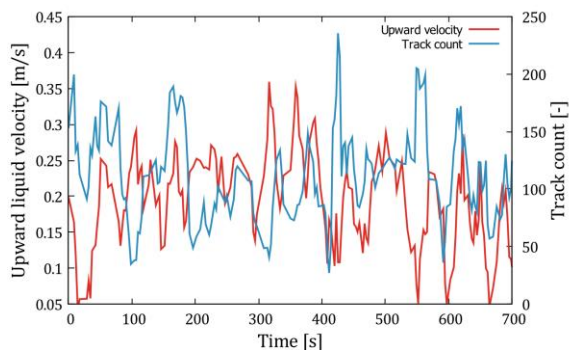


Figure 8 Correlation between liquid velocity and track count for  $U_G = 1.48$  cm/s,  $U_L = 0$  cm/s in the center of the column.

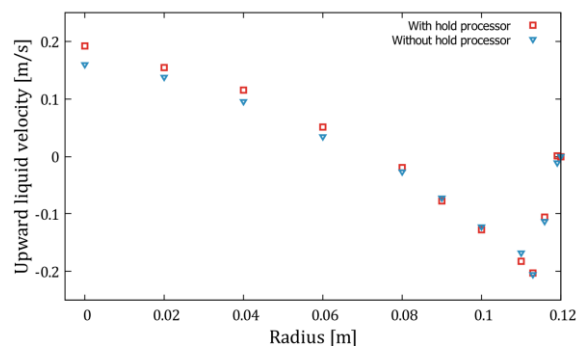


Figure 9 Results with and without hold processor for  $U_G = 1.48$  cm/s,  $U_L = 0$  cm/s

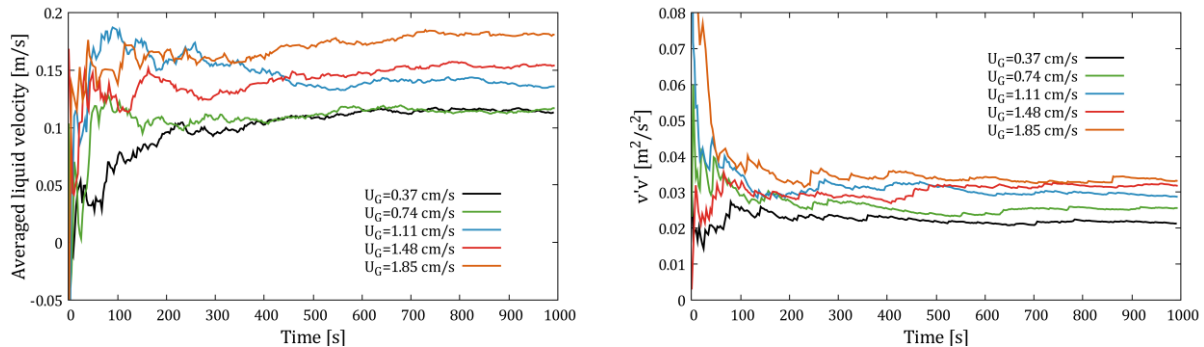
357 Another sampling bias might be obtained because the bubbles are faster moving than the  
 358 liquid as explained in the previous section. In principle, we try to catch tracer particles in  
 359 spaces between the moving bubbles. If a particle in the first picture is identified right above  
 360 a bubble and if the tracer is too slow, it will be blocked in the next picture by the ascending

361 bubble and the track is lost. However, a faster tracer would be not blocked and therefore  
 362 tracked. The same mechanism is present if a fast tracer is situated right below a bubble that  
 363 is slower ascending and, therefore, not in the measuring plane. However, the effect is  
 364 asymmetric due to the upward direction of the rising bubbles so that slower tracers will be  
 365 generally more often lost than fast tracers will. The quantification and evaluation of the  
 366 effect is difficult so that it will be not treated at this point.

### 367 3.4 Verification and validation

#### 368 3.4.1 Measuring time

369 Despite the bubble column is operating in the homogeneous regime in which the integral  
 370 gas holdup is increasing linear with the superficial gas velocity, a bubble plume with very  
 371 long time scales can be observed (Figure 10). After every change of the superficial liquid  
 372 and/or gas superficial velocity, we waited 30 minutes before the measuring campaign  
 373 began. In Figure 10, the accumulation of the time averaged liquid velocity, i.e.  $v(T) =$   
 374  $\int_T \langle v(t) \rangle dt$ , in the center plane for batch mode is shown. Even after 1000 seconds, the  
 375 averaged velocities show some changes over time. Nevertheless, the changes are rather  
 376 small so that a 1000-second measuring time was a good compromise between accuracy  
 377 and effort; additionally, a 1000-second measuring time has been also used for the optical  
 378 probe measurements (Besagni & Inzoli 2016a). Since the normal Reynolds stresses are the  
 379 variance of the single velocity components, they converge faster than the averages. The  
 380 statistical uncertainty given by  $\frac{\sigma}{\sqrt{N}}$  is for the averaged velocity below 0.001 m/s and for  $v'v'$   
 381 below 0.0003 m<sup>2</sup>/s<sup>2</sup> for all operation conditions.



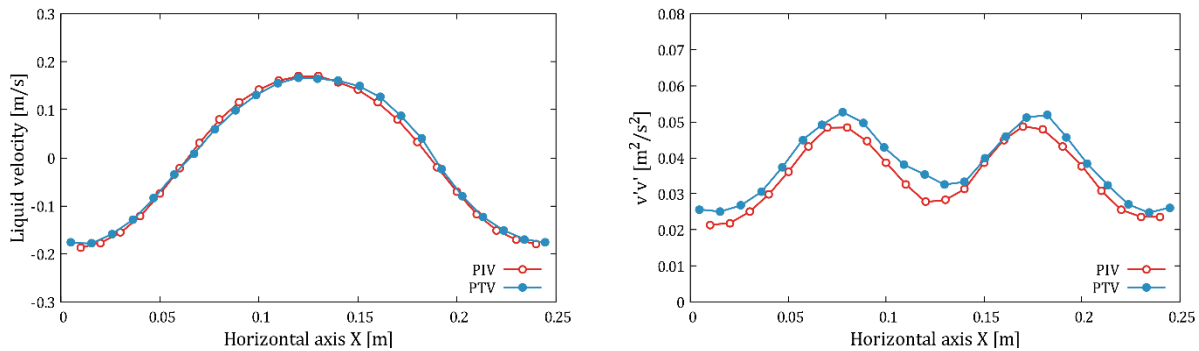
382

383 Figure 10 Accumulation of the averaged liquid velocity and  $v'v'$  over time for different  
 384 superficial gas velocities in batch mode.

#### 385 3.4.2 Comparison with PIV

386 In our previous work (Hessenkemper & Ziegenhein 2018) we compared the present PSTV  
 387 algorithm with PIV measurements in a smaller test bubble column. In this study, the tracer-  
 388 particle density was chosen in a way that both methods worked well and the spatial  
 389 resolution was adapted to the specific requirements of the specific method. Compared to

390 the present study, the seeding was distinctly higher so that the comparison of PIV and PSTV  
 391 in the following shows only that the used PSTV algorithms are valid and applicable to  
 392 bubbly flows. The results for a superficial gas velocity of 1 cm/s with comparable bubble  
 393 sizes to the present case are shown in Figure 11. The obtained liquid velocity shown in  
 394 Figure 11 a) is almost equal for both methods. For the normal component of the Reynolds  
 395 stress tensor in upward direction,  $v'v'$  shown in Figure 11 b), PSTV delivers slightly higher  
 396 values. Since PIV is using interrogation areas that function like a box filter,  $v'v'$  obtained  
 397 from PSTV measurements are higher in general, which might be the reason for that  
 398 deviation.



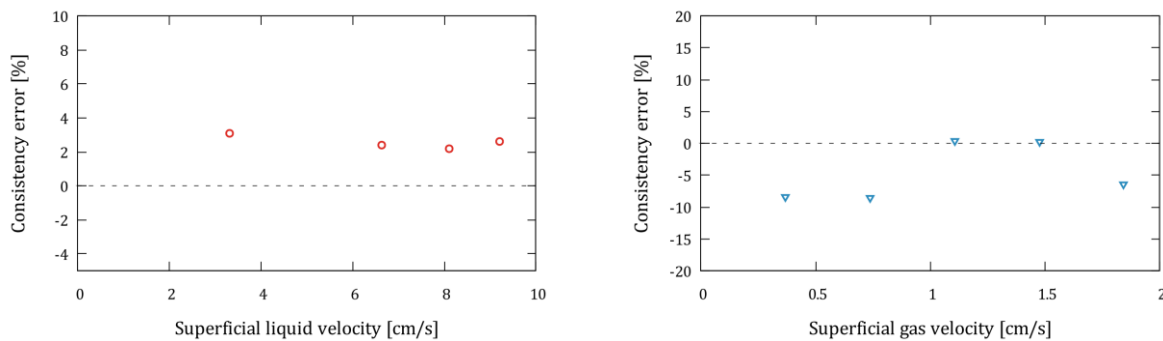
399 Figure 11 Comparison of the present PTV algorithm with PIV measurements from  
 400 Hessenkemper & Ziegenhein (2018).

### 401 3.4.3 Consistency

402 The evaluation of the present methods can be done by calculating the integral properties of  
 403 the flow with the local measurements. By integrating the local results, small systematic  
 404 errors are summed up and can be therefore easily accessed by evaluating the consistency  
 405 between the theoretical and determined properties. The strategy is as follows, with the  
 406 liquid velocity field and the void fraction profiles, which are only available for the batch  
 407 mode, from the previous measurements in the column, the superficial liquid velocity in the  
 408 bubble column can be calculated. The calculated superficial velocity should be zero in batch  
 409 mode.

410 As a basic test, we evaluate the superficial liquid velocity without gas 0.7 m above the  
 411 sparger. At 0.7 m above the sparger, we assume that inlet effects from the counter current  
 412 flow, which is distributed at the top of the column through a basin, are negligible. Under  
 413 this condition, we see an overprediction of around 3% (Figure 12 left), which is in the  
 414 range of the uncertainty of the mechanical rotameter. It should be emphasized that we only  
 415 measure half of the column and cannot consider asymmetric behaviors. Further, it should  
 416 be noted, that the consistency error is higher on the upper measuring level at 1.9 m above  
 417 the sparger. Therefore, we conclude that asymmetric inlet effects are present at this level  
 418 despite the basin of  $0.0735 m^3$  on top of the column (Figure 1), particularly at high volume  
 419 flow rates. Therefore, we focus in the following on the lower measuring position and the  
 420 results of the upper position are given in the Appendix.

421 Another picture is obtained in batch mode at the same measuring position, 0.7 m above the  
 422 sparger. Multiplying the measured liquid velocity and the measured liquid volume fraction  
 423 (Besagni & Inzoli 2016a), the integration of this product is an estimation for the superficial  
 424 liquid velocity. However, since the volume fraction and liquid velocity measurements are  
 425 almost one year apart, the correlation between these two values,  $\overline{(1-\alpha)'v'}$ , is not  
 426 included. In Figure 12 right hand side, is the volume flow obtained by integrating the  
 427 velocity profile divided by the total recirculation volume flow for batch mode as a  
 428 percentage value shown. Considering that the present measurements and the void fraction  
 429 measurements are one year apart, that we neglect the correlation  $\overline{(1-\alpha)'v'}$ , and the  
 430 general difficulty to measure liquid velocities in multiphase flows, a deviation of 10%  
 431 integral error is very acceptable.



a) Comparing the integration of the liquid velocity profile with the volume flow regulated at the pumping station for Single-phase flow, 0.7 m above sparger

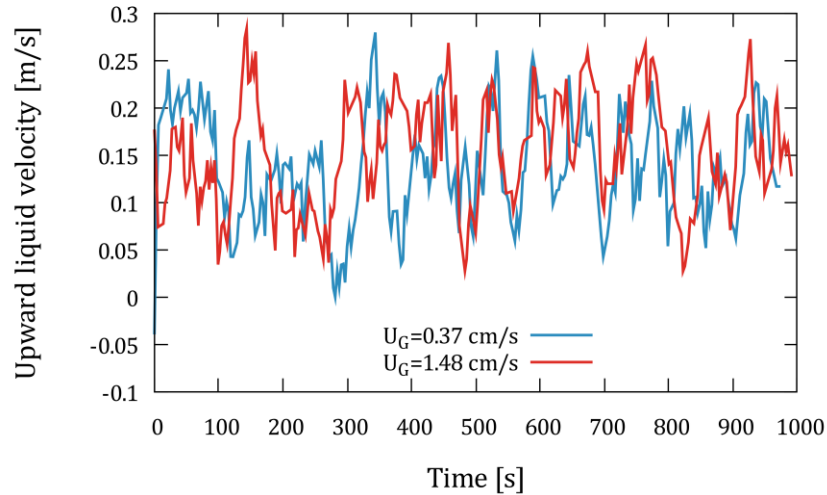
b) Consistency error calculated with the measured gas volume fraction and the liquid velocities in batch mode, 0.7 m above sparger

432 Figure 12 Consistency of the measurements. a) The error of the superficial liquid velocity  
 433 without gas for two different fill-heights of the column. b) The lack of the superficial liquid  
 434 velocity for different superficial gas velocity without counter current flow and 0.3 m fill  
 435 height.

## 436 4 Experimental results

### 437 4.1 Long-time, transient behavior

438 Despite in the pseudo-homogeneous flow regime the integral gas holdup is changing linear  
 439 with increasing superficial gas velocity (see Figure 28a, in Appendix A), a distinct transient  
 440 behavior of a center-plume at both measurement levels can be observed. The upward  
 441 liquid velocities,  $\langle v \rangle$ , in the center of the column for two different gas superficial  
 442 velocities ( $U_G = 0.32$  cm/s and 1.48 cm/s) in the batch mode are shown in Figure 13. The  
 443 transients are moving averages over 6 seconds, which is equal to a low pass filter with a  
 444 rectangular function with a size of 6 seconds, to emphasize the very long time scales, which  
 445 are characteristic for bubble plumes. In fact, from a Fourier-Transform dominant  
 446 frequencies can be obtained (Figure 14).

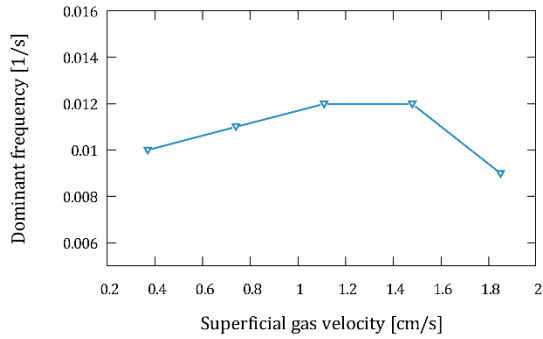


447

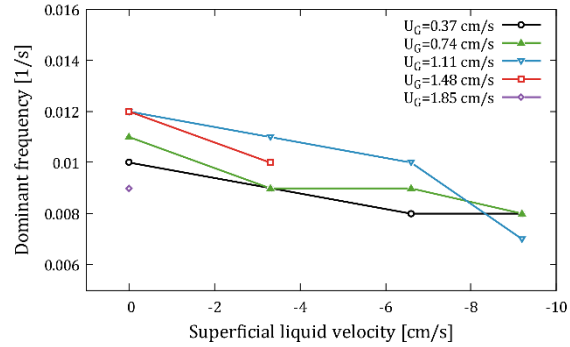
448 Figure 13 Large-scale transient behavior for  $U_G = 0.37 \text{ cm/s}$  and  $U_G = 1.48 \text{ cm/s}$  for  
 449 batch mode,  $U_L = 0 \text{ cm/s}$ , in the center of the column at the lower measuring level. The  
 450 results are moving averaged over 6 seconds. Local, instantaneous velocities can be  
 451 therefore distinctly higher.

452 The nominal frequency resolution of the Discrete Fourier Transformation is  $1/1000 \text{ 1/s}$ ,  
 453 which is poor since the dominant frequencies are in the range of  $1/100 \text{ 1/s}$  (Figure 14 left).  
 454 Nevertheless, a trend can be observed that the plume frequency is increasing with  
 455 increasing superficial gas velocity, as often reported for tabletop bubble columns. After the  
 456 bubble plume frequency is increased, the frequency is decreasing for the highest superficial  
 457 gas velocity, which comes close to the flow regime transition (Section 2.2). Such a decrease  
 458 needs to be further investigated due to the poor frequency resolution. Nevertheless, the  
 459 decrease in frequency is in line with the observations of the authors that at this superficial  
 460 gas velocities a very large amount of small bubbles exist, compared to a pure bubble plume  
 461 with large bubbles at lower superficial gas velocities.

462 Another observation is that with increasing superficial liquid velocity in the counter-  
 463 current flow setup (Figure 14 right), the frequencies are decreasing for all gas velocities.  
 464 Probably, the rotation of the counter-current liquid flow due to inlet effects hinders the  
 465 natural rotation of the bubbly flow, as discussed in the next section, and therefore  
 466 influences the plume frequency. However, the counter-current mode destabilizes the  
 467 homogeneous flow regime in general. The relationship between plume frequency and the  
 468 prevailing flow regime is a matter of future studies.



(a) Batch mode

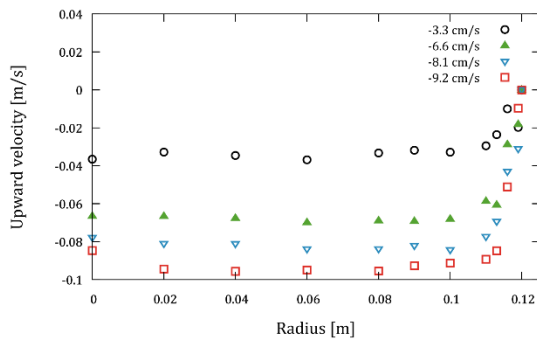


(b) Counter-current mode

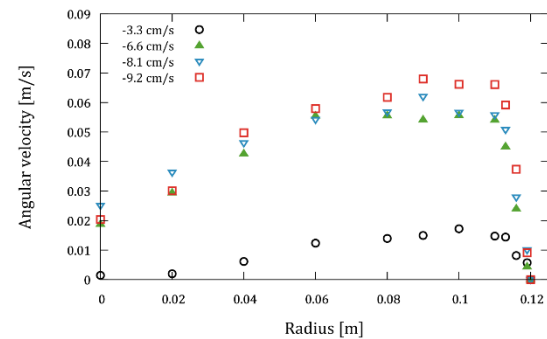
469 Figure 14 Dominant frequencies, obtained by Fourier-Transform of instantaneous  
 470 velocities, in the batch mode with varying superficial gas velocities (a) and in the counter-  
 471 current mode with varying superficial liquid velocities for different superficial gas  
 472 velocities,  $U_G$ , (b) evaluated from the velocity transients determined in the center of the  
 473 column.

#### 474 4.2 Time averaged liquid velocity profiles

475 The averaged liquid velocity profile,  $\bar{v}$  (cf. Eq. (2)), for the single-phase flow without gas is  
 476 flat in the center with a steep slope towards the wall (Figure 15a). The single-phase flow  
 477 Reynolds number calculated with the pipe diameter as characteristic length scale is ranging  
 478 from around 9,000 to 20,000. As expected, the profiles are just shifted to higher absolute  
 479 velocities with increasing flow rate. Due to the radial inflow in the basin on top of the  
 480 column, the water is rotating in it. This rotation can be clearly seen in the angular velocity  
 481 (Figure 15b). From visual observation, this circular current is preserved towards the  
 482 bottom of the column. In the angular velocity, an asymmetry can be seen since the sign  
 483 change is not in the center of the column for superficial liquid velocities above -3.3 cm/s,  
 484 which might explain the inconsistent behavior shown in Figure 12a for a fill height of 0.3 m.



(a) Single-phase flow

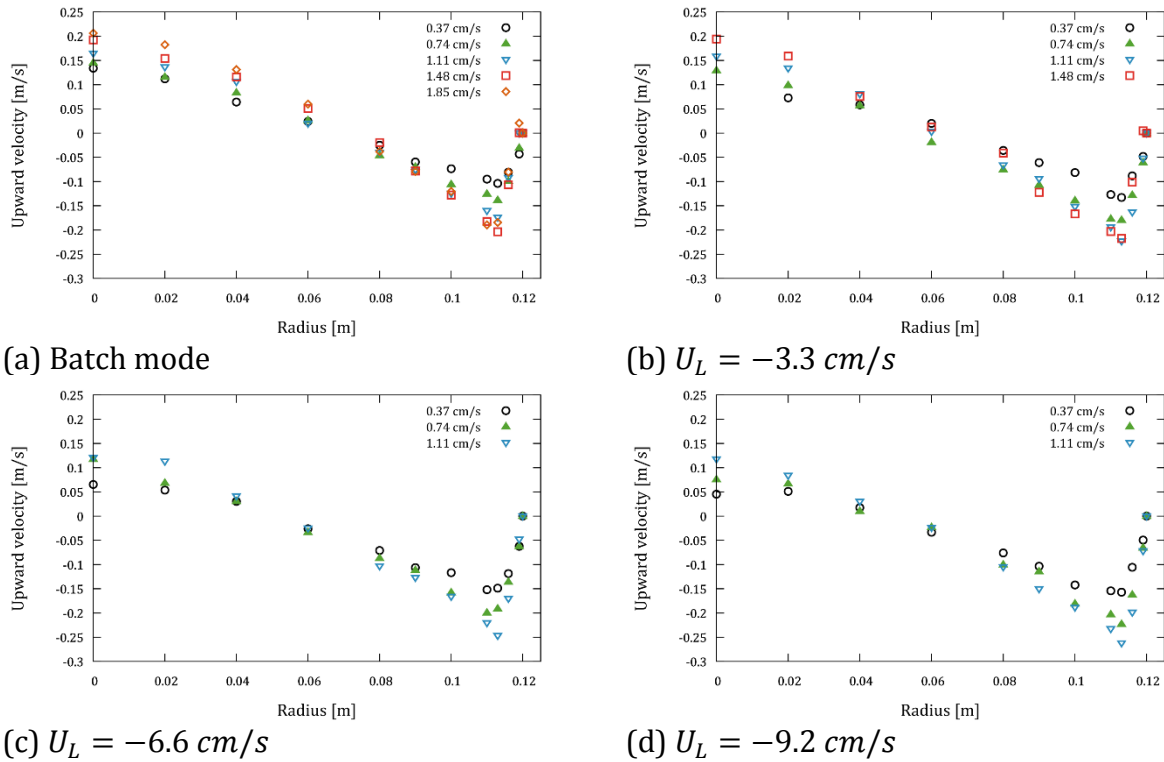


(b) Single-phase flow

485 Figure 15 Averaged velocities without gas ( $U_G = 0$  cm/s) at different superficial liquid  
 486 velocities. a) The upward velocity and b) the angular velocity against the column radius.

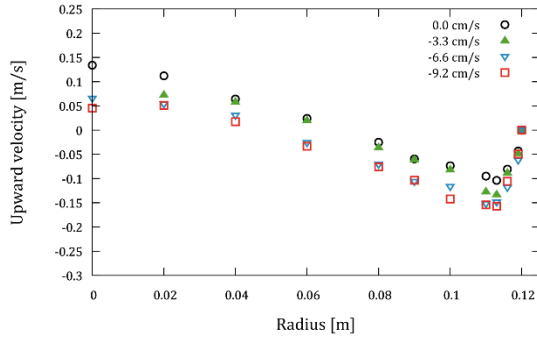
487 The averaged upward liquid velocities for all operations points are compared in Figure 16.  
 488 With increasing superficial gas velocity, the gradients in the liquid profiles are getting

489 steeper, which can be nicely seen for the batch mode. For all operation points, the point of  
 490 minimum velocity is situated around 0.075 mm away from the wall. The shape of the liquid  
 491 velocity profile is as the one reported in the pioneering study of Ueyama & Miyauchi  
 492 (1979). The liquid phase flows upward in the center of the column, it becomes zero at an  
 493 intermediate radial position (close to  $r/\sqrt{2}$ ) and, finally, it flows downward near the wall.  
 494 The reader may refer to Appendix B for the data obtained at  $h = 1.9$  m above the gas  
 495 sparger, where similar consideration can be applied.

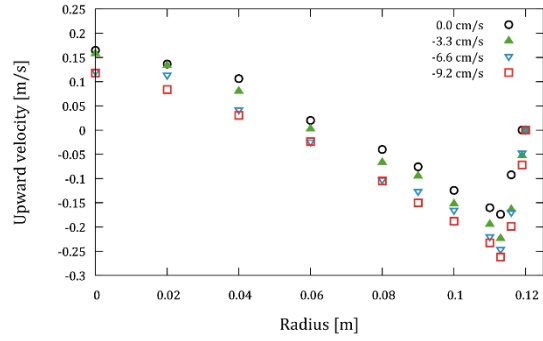


496 Figure 16 Averaged upward liquid velocities for different superficial gas velocities at  
 497 different superficial liquid velocities,  $U_L$ , 0.7 m above the gas sparger.

498 The influence of the counter-current flow is emphasized in Figure 17. Overall, the velocity  
 499 profiles are just shifted downwards due to the superficial liquid velocity. This observation  
 500 is consistent with our previous observations that are summarized in Appendix A (Figure  
 501 28, 29 and Figure 30). Further, this is also the assumptions made by Trivedi et al. (2018),  
 502 who predict the velocity field in counter-current bubble columns, which is correct for the  
 503 present flow configurations.



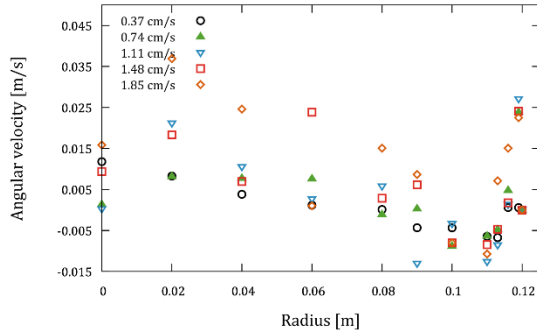
(a)  $U_G = 0.37 \text{ cm/s}$



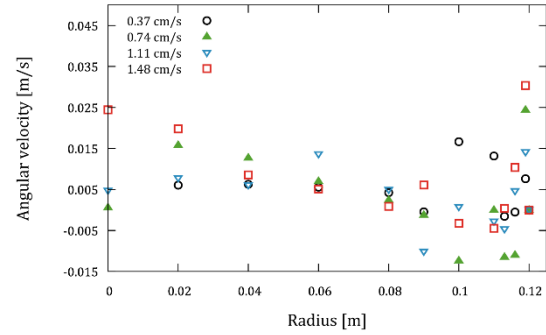
(b)  $U_G = 1.11 \text{ cm/s}$

504 Figure 17 Averaged upward liquid velocities for different counter-current flow setups at  
 505 different superficial gas velocities 0.7 m above the gas sparger.

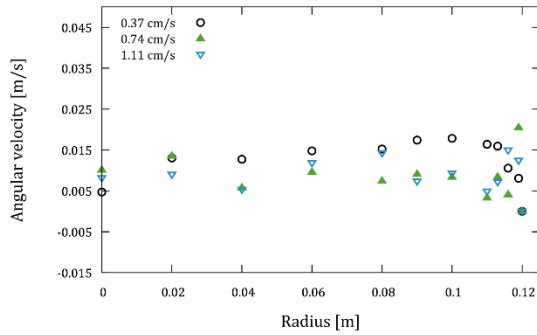
506 The angular velocity, which is for the present measuring setup equal to the measured  
 507 horizontal liquid velocity due to the small observation plane (cf. Section 2.2), is changing  
 508 distinctly with increasing liquid superficial velocity (Figure 18). The bubbly flow generates  
 509 a clear circulating flow, which is changing its direction several times towards the center.  
 510 This counter-current angular flow less influences when the liquid velocity is increased  
 511 to  $U_L = -3.3 \text{ cm/s}$ . Due to the radial inflow in the basin on top of the column, the  
 512 circulating flow of the liquid inflow (Figure 15) dominates the bubbly flow at  $U_L =$   
 513  $-6.6 \text{ cm/s}$  and  $U_L = -9.2 \text{ cm/s}$ .



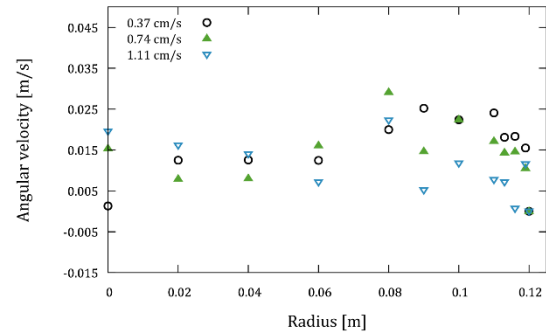
(a) Batch mode



(b)  $U_L = -3.3 \text{ cm/s}$



(c)  $U_L = -6.6 \text{ cm/s}$

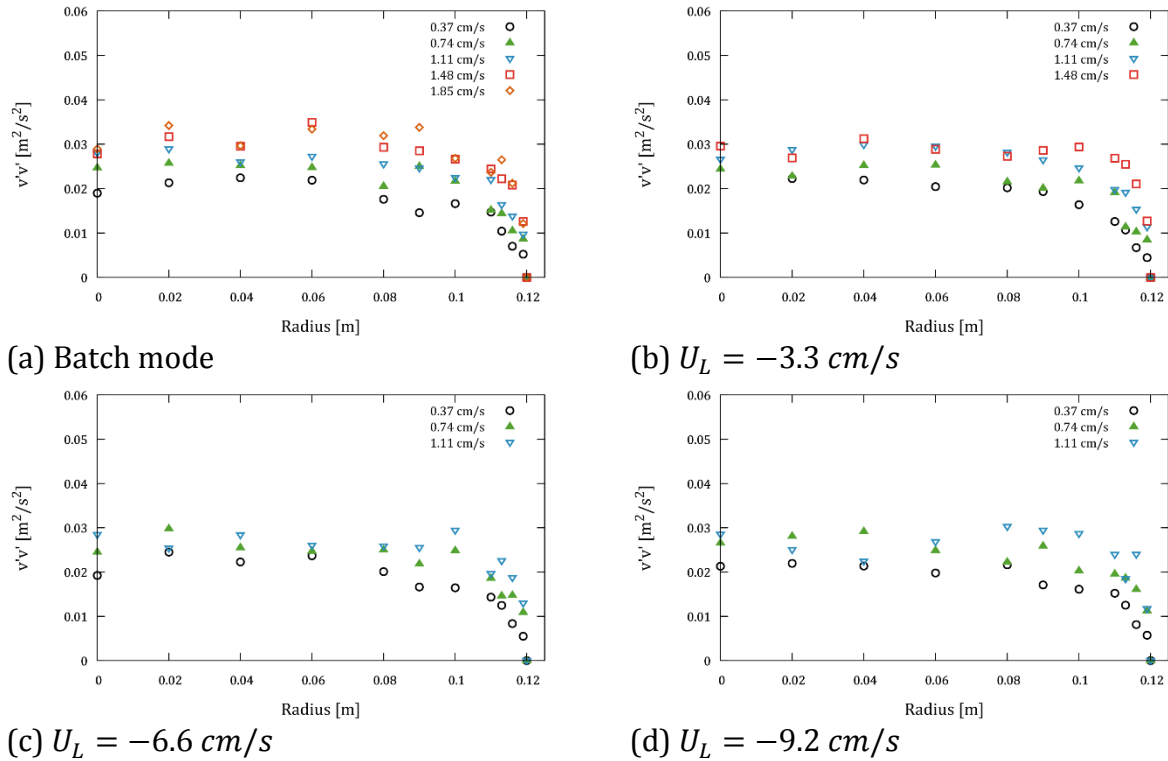


(d)  $U_L = -9.2 \text{ cm/s}$

514 Figure 18 Averaged angular liquid velocities for different superficial gas velocities at  
515 different counter-current flow setups 0.7 m above the gas sparger.

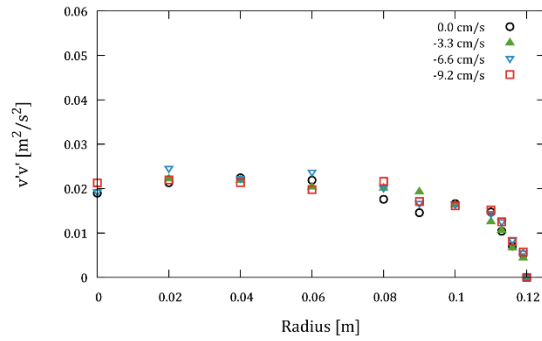
516 **4.3 Normal Reynolds stresses**

517 The normal Reynolds stress tensor component in upward direction,  $v'v'$ , is almost zero for  
518 the single-phase liquid downflow. Increasing the gas flow rate,  $v'v'$  is increasing (Figure  
519 19) for all counter current flow rates. This increased  $v'v'$  rate might have two origins. First,  
520 the gas hold-up is increasing, which increases the small-scale turbulence. Second, the  
521 plume frequency is increasing with increasing superficial gas flow rate (Figure 14) so that  
522 the very large transient scales increase. The almost equal  $v'v'$  obtained for  $U_G = 1.48 \text{ cm/s}$   
523 and  $U_G = 1.85 \text{ cm/s}$  in batch mode can be explained by the decreasing plume frequency at  
524  $U_G = 1.85 \text{ cm/s}$  (Figure 14), which indicates a damping of the very large transient scales.

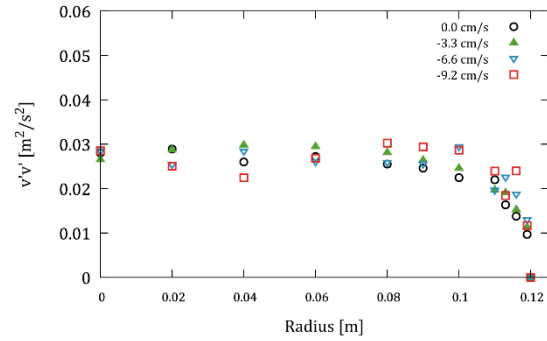


525 Figure 19 Normal Reynolds stresses in upward direction for different superficial gas  
 526 velocities at different counter-current flow setups 0.7 m above the gas sparger.

527 Certainly, the counter-current liquid flow is increasing the gas hold-up (see Figure 28a in  
 528 Appendix A) so that in principle  $v'v'$  should be increasing with increasing superficial liquid  
 529 velocity. Surprisingly,  $v'v'$  is not or only minor changing for different superficial liquid  
 530 velocities (Figure 20). This might be explained by the damping of the plume frequency and  
 531 therefore the large scales when the superficial liquid velocity is increased (Figure 14). This  
 532 reduction of the large scales might cancel out the effect of higher gas volume fractions in  
 533 total. In fact, with the method discussed in the next section to separate the large and small  
 534 scale, it will be shown that a filtered  $v'v'$  is increasing with increasing superficial liquid  
 535 flow rate.



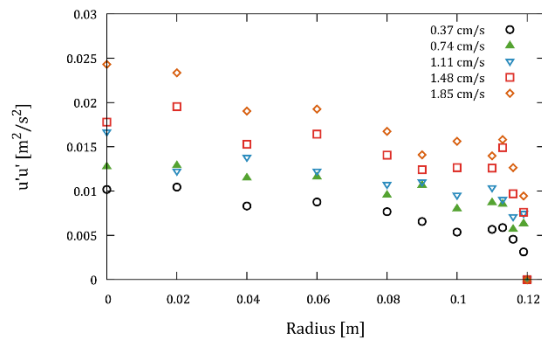
(a)  $U_G = 0.37 \text{ cm/s}$



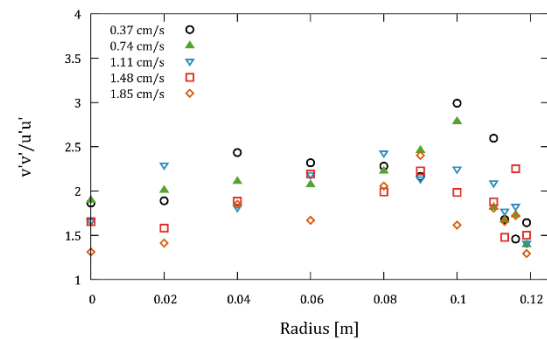
(b)  $U_G = 1.11 \text{ cm/s}$

536 Figure 20 Normal Reynolds stresses in upward direction for different counter-current flow  
 537 setups for a superficial gas velocity of  $0.37 \text{ cm/s}$  (a) and  $1.11 \text{ cm/s}$  (b),  $0.7 \text{ m}$  above the gas  
 538 sparger.

539 The angular component of the Reynolds stress tensor ( $u'u'$ ) (Figure 21) is behaving very  
 540 similar to the upward direction. Certainly, the large-scale fluctuations are also present in  
 541 angular direction so that  $u'u'$  is also influenced by the plume frequency. This behavior of  
 542 the system might also significantly influence the ratio of the upward and angular  
 543 component (Figure 21).  $v'v'$  is dominating around  $2 \text{ cm}$  away from the wall whereas  
 544 towards the center the ratio is decreasing towards  $1.5$ . Changing the superficial liquid and  
 545 gas velocity does not change the ratio significantly.



(a) Batch mode



(b) Batch mode

546 Figure 21 Normal Reynolds stresses in angular direction for the batch mode (a) and the  
 547 ratio of normal upward and angular tensor components in batch mode (b),  $0.7 \text{ m}$  above the  
 548 gas sparger for different superficial gas velocities.

#### 549 4.4 Filtered normal Reynolds stresses

550 Filtering the transient velocity results is a method to mask the influence of the large-scale  
 551 fluctuations of the meandering bubble plume. The intention of this process is to study the  
 552 smaller scales that might be dominated by the bubble-induced turbulence. Due to the filter,  
 553 the scales are separated as is usually done in LES. The similarities to LES are obvious, due  
 554 to the measurement concept of recording planes in bursts; a filter in space can be used that  
 555 is accessible at different time steps. However, the choice of potential filter sizes is limited

556 due to the restrictions of the measurements. Therefore, for all operation points the same  
 557 filter will be used and the focus will not be on the absolute value of the filtered turbulent  
 558 kinetic energy but on the change with the volume fraction.

559 Looking at the bubble-induced turbulence scale, the important effects are on a length scale  
 560 comparable to the bubble size (Ma et al. 2017). In the present setup, the bubbles are  
 561 between 3 and 6 mm large (Besagni and Inzoli, 2016a) so that the 6 mm width of the  
 562 measurement plane is a good choice for the filter in angular direction. We choose the height  
 563 of the filter in stream-wise direction to the complete height of the measuring plane – 25.3  
 564 mm – in order to increase the statistics compared to a 6 mm x 6 mm box. However, at lower  
 565 void fraction where a very large amount of tracers is trackable, similar results are obtained  
 566 with a 25.3 mm x 6mm and a 6 mm x 6mm box.

567 The time scale of the bubble-induced turbulence might be connected to the ratio of slip  
 568 velocity and bubble size (Ma et al. 2017). With a slip around 23 cm/s (Tomiyama 2002)  
 569 and an averaged bubble size around 4 mm, a characteristic frequency for the bubble-  
 570 induced turbulence is found to be around 60 Hz. Lance & Bataille (1991) measured the one  
 571 dimensional energy spectra in homogenous bubbly flows with 5 mm bubbles and reported  
 572 the significant range between 100 and 1000 Hz. Averaging the information in time over the  
 573 set of 10 pictures recorded each with 1000 Hz, a total frequency of 100 Hz is obtained,  
 574 which is near the estimated frequency of 60 Hz and in the measured range from Lance &  
 575 Bataille. Summarizing, a reasonable box filtering process is obtained by averaging the  
 576 obtained velocities over the measuring plane of 6 mm times 25.3 mm and over 0.01  
 577 seconds with the focus on the bubble-induced turbulence.

578 Based on the turbulent kinetic energy, it is possible to state that the suggested filter  
 579 satisfies the following equality:

$$\langle v'v' \rangle_{Total} = \langle v'v' \rangle_{HighPassFilter} + \langle v'v' \rangle_{LowPassFilter} \quad (5)$$

580 From the explanations above, the low pass filter would be

$$\langle v'v' \rangle_{LowPassFilter} (R_j) = \frac{1}{T} \int_{1000s}^{0s} \left( \bar{v}(R_j) - \omega \langle v \rangle (T_i, R_j) \right)^2 dt, \quad (6)$$

581 with the formulations given in Equation (1) - (3). This low pass filter means that the  
 582 turbulent kinetic energy is calculated with the overall averaged velocity,  $\bar{v}(R_j)$ , and the  
 583 averaged velocity over the 10 burst and the measuring plane  $\langle v \rangle (T_i, R_j)$ , which is  
 584 weighted by the hold processor.

585 The high pass filter is than only the turbulent kinetic energy inside the 10 bursts. This can  
 586 be obtained by subtracting the low pass filter from the total value, or by calculating the  
 587 value from the measured values. In the following, the calculation will be shown, and  
 588 Equation (5) will be used to check the results. At first, the filtered turbulent kinetic energy

589 is obtained by calculating the averaged velocity over the set of 10 pictures,  $\langle v \rangle$  (cf.  
 590 Equation (1)); afterwards, the fluctuations are calculated with this averaged velocity for  
 591 every tracked particle:

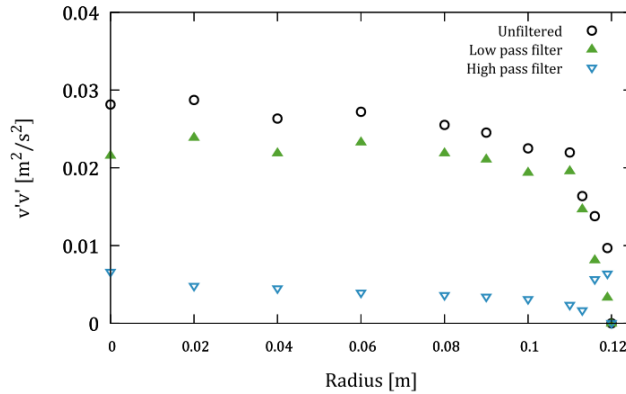
$$\langle v'v' \rangle_{HighPassFilter} (T_i, R_j) = \frac{1}{9} \int_{T_i + \frac{1}{100}s}^{T_i} \int_{R_j} \left( \langle v \rangle - v(x, t)_{R_j} \right)^2 dAdt, \quad (7)$$

592 In the end, the turbulent kinetic energies are averaged over the complete 1000 seconds  
 593 measuring time, which includes 500 sets of 10 pictures per measuring point:

$$\bar{v}(R_j) = \frac{1}{T} \int_{1000s}^{0s} \omega \langle v'v' \rangle (T_i, R_j) dt, \quad (8)$$

594 with  $\omega$  again the weight from the hold processor as discussed in Section 3.3. The sum of  
 595 both filter process is equal to the total value of the turbulent kinetic energy, as expected.  
 596 Certainly, the made assumptions regarding the filter size in space and time are rough so  
 597 that the absolute values that will be obtained with the filtering process should be  
 598 interpreted with care. Nevertheless, the change of the obtained values with the volume  
 599 fraction is in the focus, which is less sensitive to the filter sizes when they are in the range  
 600 of the bubble-induced turbulence.

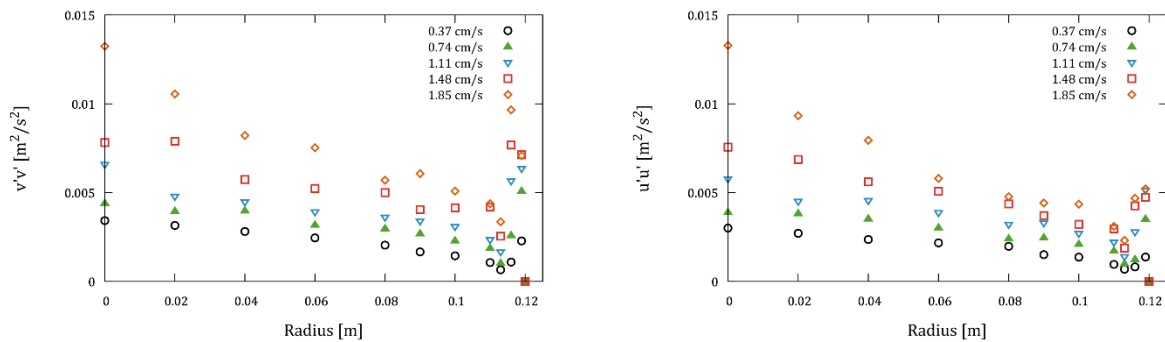
601 The filtered values are compared to the unfiltered in Figure 22. As expected, due to the  
 602 non-homogenous distribution of the gas fraction and the resulting bubble plume, the high-  
 603 energy scales are the very low ones causing the low pass filter to be distinctly higher. The  
 604 high pass and low pass filtered values approach each other towards the walls where the  
 605 large scales are damped. When the y-axis is scaled properly for the high pass filtered values  
 606 (Figure 23), these values increase towards the center whereas the values for the low pass  
 607 filtered values are more or less constant from  $r = 0.1$  on. The high pass filtered  $v'v'$  values  
 608 increase in the same amount as the gas void fraction values towards the center of the  
 609 column, which will be discussed in detail below. This is a hint that our filtering actually is in  
 610 the turbulent scales that depend directly on the gas void fraction. On the other hand, the  
 611 low pass filtered values are dominated by the global flow so that these values are almost  
 612 not influenced by the local void fraction distribution.



613

614 Figure 22 Comparison of filtered and unfiltered turbulence data for a superficial gas  
 615 velocity of 1.11 cm/s in batch mode.

616 From now on only the high pass filtered values are in the focus. the obtained filtered values  
 617 over the radius for all batch mode operation-points are shown in Figure 23. Compared to  
 618 the unfiltered values, the filtered values are increasing nicely with the superficial gas  
 619 velocity. Near the wall, they have a maximum, which might be explained due to the high  
 620 shear rates there. Surprisingly, near the velocity minimum, the filtered values have a  
 621 minimum. From this point, the values for all operation points are increasing steadily  
 622 towards the center.

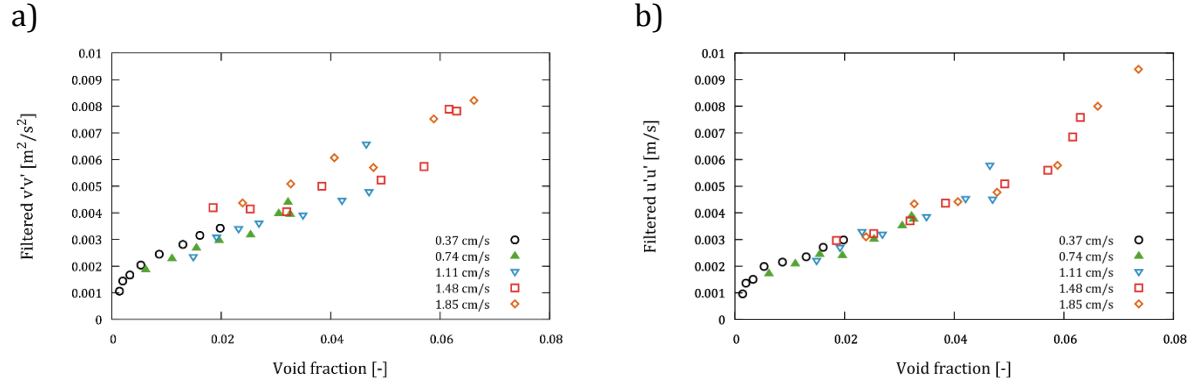


(a) Batch mode

(b) Batch mode

623 Figure 23 Filtered normal Reynolds stresses in upward (a) and angular (b) direction for  
 624 batch mode at different superficial gas velocities 0.7 m above the gas sparger.

625 With the volume fraction profiles measured for the batch mode by Besagni & Inzoli  
 626 (2016a), every local filtered value from Figure 23 can be assigned to a local volume fraction  
 627 (Figure 24). Since the volume fractions were measured at slightly different position, the  
 628 void fraction values were interpolated using the void fraction profile by second order to the  
 629 locations where the liquid velocities had been measured. Since the wall effects are not in  
 630 the focus, only the values from 0 to 0.1 m radius will be considered in the following. The  
 631 values obtained for different superficial gas velocities at different position are overlapping  
 632 for  $v'v'$  and  $u'u'$ . Moreover, they behave almost linear with a strongly decreasing trend  
 633 towards zero volume fraction.

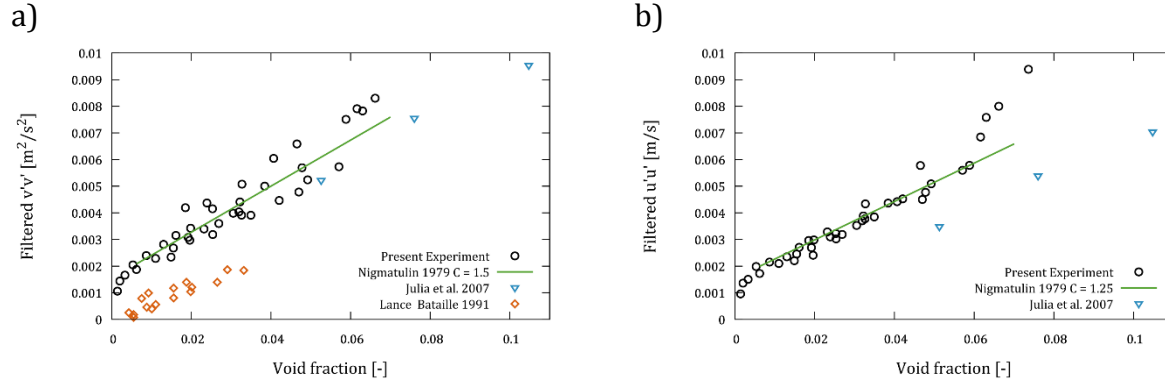


634 Figure 24 Filtered normal Reynolds stresses in upward (a) and angular (b) direction for  
 635 batch mode at different superficial gas velocities plotted against the gas volume fraction.

636 A linear trend of the bubble-induced turbulence with increasing volume fraction,  
 637  $\alpha$ , for pure homogenous flow without a turbulent background flow was for example  
 638 postulated by Nigmatulin (1979) with the formulation

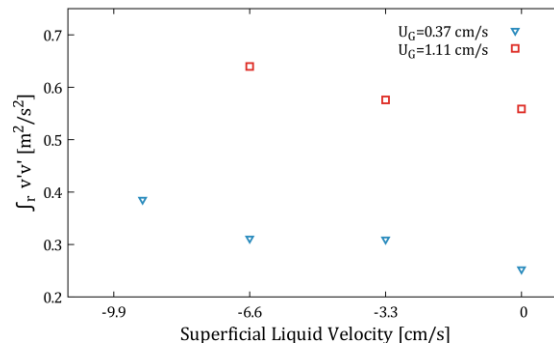
$$k_{L,BIT} = C|\vec{v}_{rel}|^2\alpha. \quad (9)$$

639 With  $v_{rel}$  the slip velocity, which is fixed to 23 cm/s in the following. For the model  
 640 constant  $C$  different formulation exist; e.g., Lopez de Bertodano et al. (1996) used a  
 641 formulation connected to the virtual mass coefficient,  $C_{VM}$ ,  $C = 0.5C_{VM}$  or Julia et al. (2007)  
 642 used  $C = 1$  to fit their measured  $v'v'$  values. For the present results, a model constant of 1.5  
 643 for  $v'v'$  and 1.25 for  $u'u'$  would fit the slope for increasing the volume fraction (Figure 25).  
 644 However, the results from Figure 24 indicate a non-linear onset of the turbulence at very  
 645 low volume fractions. Therefore, we add a constant factor to Equation (9) to cover the  
 646 linear trend from 0.005 gas volume fraction (Figure 25). This constant factor might be  
 647 determined by the chosen filter size and is therefore not of significance at this point.  
 648 However, the measurements of Julia et al. (2007) are close to the present measurements in  
 649 absolute height and slope. The measurements of Lance & Bataille (1991) are a factor of two  
 650 lower but with a similar slope. It should be noted that both, the measurements of Julia et al.  
 651 and Lance & Bataille, are executed in small table top bubble columns in a pure homogenous  
 652 regime without a bubble plume and an almost monodisperse bubble size distribution,  
 653 which is substantially different to the present experimental setup.



654 Figure 25 Filtered Reynolds stresses in upward and angular direction compared to other  
 655 experiments in batch mode and Eq. (9).

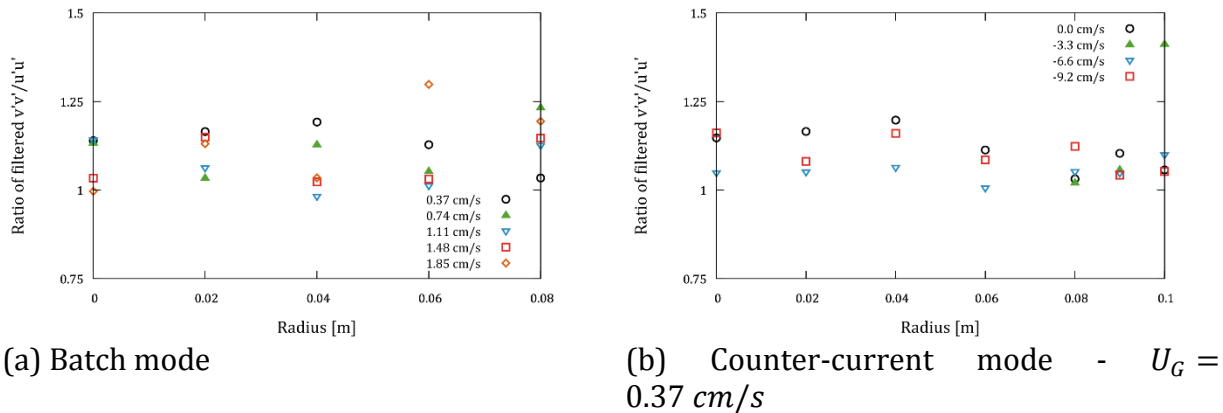
656 The inconsistency described in the previous section of constant  $v'v'$  values with increasing  
 657 superficial liquid velocity and therefore increasing volume fraction (Figure 20) is  
 658 eliminated by using the filtered values. In Figure 26 the integral of the filtered  $v'v'$  over the  
 659 radius is shown in order to emphasize the total change of  $v'v'$  with the increasing liquid  
 660 volume flow rate. As expected, the filtered  $v'v'$  results are increasing with increasing  
 661 superficial liquid velocity so that the assumption that the damping of the large scales with  
 662 increasing superficial liquid velocity are counteracting the increasing trend of the small  
 663 scales with the volume fraction is reasonable. Unfortunately, for the counter-current flow  
 664 setup no volume fraction measurements are available so that these values cannot be added  
 665 to Figure 25.



666  
 667 Figure 26 Integrated  $v'v'$  over the column radius for different counter-current flow setups  
 668 for a superficial gas velocity of 0.37 cm/s and 1.11 cm/s, 0.7 m above the gas sparger. The  
 669 superficial liquid velocity is increasing towards negative numbers.

670  
 671 The ratio of the small scale  $v'v'$  and  $u'u'$  (Figure 27) are distinctly smaller than the non-  
 672 separated ones (Figure 21) and more or less constant over the radius between values of  
 673 1.25 and 1.0. In the literature different values for the ratio can be found ranging from 2.0

674 (Julia et al. 2007) to 1.0 (Lance & Bataille 1991). The ratio seems to be not significantly  
 675 influenced by the superficial liquid velocity (Figure 27 b).



676 Figure 27 Ratio of  $v'v'$  and  $u'u'$  for different superficial gas velocities in batch mode (a) and  
 677 for different superficial liquid velocities at  $U_G = 0.37 \text{ cm/s}$  (b), 0.7 m above the gas  
 678 sparger.

## 679 5 Conclusions, outcomes and outlooks

680 Data sets that include the void fraction, bubble size, and liquid velocity are vital for  
 681 validating CFD codes in bubbly flows. In particular, data sets for different facility sizes are  
 682 important to validate the capability of present CFD for upscaling. While some data exist for  
 683 tabletop bubble columns, complete data sets for larger-scale bubble columns are rare. In  
 684 the present study, prior measurements of the void fraction and bubble size (Besagni and  
 685 Inzoli, 2016a) were completed with liquid velocity and basic turbulence measurements for  
 686 a pilot-scale bubble column in batch and counter-current flow mode.

687 The measurement setup was as simple as possible by using a shadowgraph technique and  
 688 tracking added particles with a *PTV* algorithm (Hessenkemper & Ziegenhein 2018). The  
 689 absence of lasers allowed us to measure the velocity in a large-scale lab where the pilot-  
 690 scale column was built. Measurements up to an integral gas holdup of around 8 percentage  
 691 were possible in the 24 cm diameter bubble column. In total, 15 measuring points, 5 in  
 692 batch and 10 in counter current flow mode, at 2 different heights were investigated.

693 Despite the integral gas holdup is increasing linearly, which is usually referred as  
 694 homogenous regime, a distinct transient behavior was observed. Relatively long time  
 695 frequencies in the range of 1/100 Hz were identified. Similar but much shorter frequencies  
 696 are often described for rectangular columns with a center gas sparger. In principle, the  
 697 used industrial spider gas sparger is a scale-up of such setups to round pilot-scale columns.  
 698 The general trend of an increasing frequency with increasing superficial gas velocity was  
 699 also found in the present study. However, the frequency is dropping for the highest volume  
 700 fraction, which might be explained by a higher bubble dispersion that hinders the plume.  
 701 Increasing the counter current liquid flow, the frequencies are decreasing for all gas

702 volume flows. It is often reported in the literature that bubble plumes show an asymmetric  
703 behavior so that they might prefer one side of the bubble column. In the present work, only  
704 measurements were conducted along one radial coordinate so that a potential asymmetric  
705 behavior is not covered by the data. This should be considered when the data is used for a  
706 potential model validation.

707 Increasing the gas flow rate in batch mode leads to an increasing strength of the  
708 recirculation, which is expressed by higher shear rates in the vertical liquid velocity.  
709 Increasing the counter current flow only shifts the liquid velocity profiles downward  
710 without a distinct impact on the time averaged shear rates. From the angular velocity, we  
711 found a distinct counter current circulating flow in batch mode, which is dominated,  
712 however, by the rotation of the counter-current liquid flow. The rotating counter-current  
713 liquid flow is very likely an inlet effect.

714 The normal Reynolds stress components are the summation of the large-scale frequencies  
715 induced by the column geometry and the bubble induced turbulence. The normal stresses  
716 are increasing with increasing the superficial gas velocity, as expected. However, when the  
717 superficial liquid velocity is increased, the values remain almost constant. Since the gas  
718 holdup is higher in counter current flow, a higher turbulence level was expected. However,  
719 the damping of the large-scale frequencies due to the counter current flow compensated  
720 this trend. A filtering technique was therefore introduced in order to separate these two  
721 effects on the turbulence level.

722 The filtering method, which is proposed on findings from previous measurements and  
723 evaluations of DNS data, allowed us to investigate the trend of a filtered turbulence. The  
724 filtering was designed in order to see the bubble-induced turbulence for the different flow  
725 setups. Indeed, it was found that the filtered turbulence level is increasing with the counter  
726 current flow setup, as expected, due to the higher gas void fraction. The increase is beyond  
727 the single flow turbulence level found with zero superficial gas velocity.

728 The previous local gas void fraction measurements allowed us to plot the filtered  
729 turbulence against the gas void fraction. The results obtained for different superficial gas  
730 velocities fall on a single linear trend line, which was proposed theoretically in the past.  
731 This linear trend was previously confirmed for measurements in small tabletop columns in  
732 absolute homogenous, specifically monodispersed bubble-size distributions and flat liquid  
733 velocity profiles, flow conditions. However, the present results reveal an onset of the  
734 turbulence at low void fractions so that the linear trend is not valid at very low bubble  
735 concentrations. This onset is in line with previous evaluation of *DNS* data (Ma et al. 2017)  
736 and might be due a misaligned balance of turbulence production and dissipation at the  
737 bubbles. All in all, the similarity of the results obtained in small-scale, homogenous bubbly  
738 flows and the present setup is an argument that bubble induced turbulence models  
739 obtained from the simplified homogenous setups are applicable to large scale facilities and  
740 can be therefore used for upscaling.

741 **6 Acknowledgement**

742 This work was partially funded by the Deutsche Forschungsgemeinschaft (DFG) under the  
743 project number 335448239.

744

## 746 A. Fluid dynamics in the bubble column

747 Gas holdup ( $\epsilon_G$ ), local gas volume fraction ( $\epsilon_{G,Local}$ ), absolute bubble velocity ( $v_b$ ) and BSDs  
748 were measured by Besagni & Inzoli (2016a) beforehand with a bed expansion technique, a  
749 double fiber optical probe and image analysis, respectively. Detailed information  
750 concerning the used instrumentation, methods, and uncertainties can be found in the  
751 descriptions of Besagni & Inzoli (2016a). The results are shortly summarized in the  
752 following to help the reader to understand the discussions in the result section.

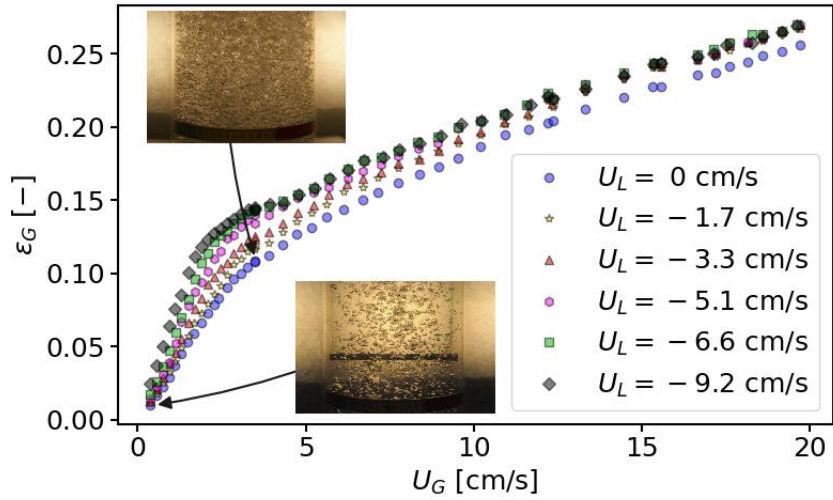
753 Figure 28 displays the gas holdup curves and the flow regime transitions ( $\epsilon_{G,trans}$  and  
754  $U_{G,trans}$ ), between the homogeneous and the transition flow regimes for the batch and  
755 counter-current mode. The liquid velocity measurements were conducted up to a void  
756 fraction of 7.55 % at  $U_L = -9.2$  cm/s. In this region, the gas holdup is monotonically  
757 increasing; however, due to the large sparger holes, a polydisperse bubbly flow is present  
758 with large bubbles (Figure 29). Moreover, the gas void fractions profiles (Figure 30) show a  
759 center peak. Since a homogenous flow regime is usually associated with a monodisperse  
760 BSD and a flat void fraction profile, the present regime is called pseudo-homogenous flow  
761 regime.

762 The linear behavior of the gas holdup with the superficial gas velocity is changing at the  
763 transition point to a pure inhomogeneous regime. In the inhomogeneous regime, larger gas  
764 structures can escape the column so that the slope of the holdup is lower compared to the  
765 pseudo-homogenous regime. A regime transition theory based on the linear stability  
766 analysis of the local force balance is for example given by Lucas et al. (2005). The transition  
767 from (pseudo-) homogenous to inhomogeneous is usually fluent so that an intermediate  
768 regime, the transition regime, can be identified. Methods to identify the transition point are  
769 for example discussed by Besagni et al. (2018).

770 The counter-current flow has the effect that the absolute bubble velocity is reduced (Figure  
771 30f) so that the local gas void fraction increases (Figure 30e). Therefore, the slopes of the  
772 gas holdup curves in the pseudo-homogenous regime are steeper when the superficial  
773 liquid velocity is increased (Figure 28a). This leads to an earlier transition with respect to  
774 the superficial gas velocity; but, the transition occurs at higher gas holdups. Since the  
775 regime transition is usually connected to coalescence events, this shift of the transition  
776 point towards higher gas holdups might be connected to the BSDs produced by the spider-  
777 sparger, which are less influenced by the counter-current flow.

778 Following the stability analysis of Lucas et al. (2005) bubbles smaller than 5.8 mm have a  
779 positive lift force coefficient (Tomiya et al. 2002) and travel to the column wall and,  
780 therefore, stabilize the flow regime. That small bubbles accumulate at the wall was indeed  
781 identified in the experiments (Besagni & Inzoli 2016a) (Figure 29). However, the  
782 observations in the experiments might be covered by coalescence/break-up events of the

783 bubbles, so that these results are only a hint of the stability of the bubble column. Empirical  
784 correlations for the stability of bubble columns are summarized by Besagni et al. (2018).  
785

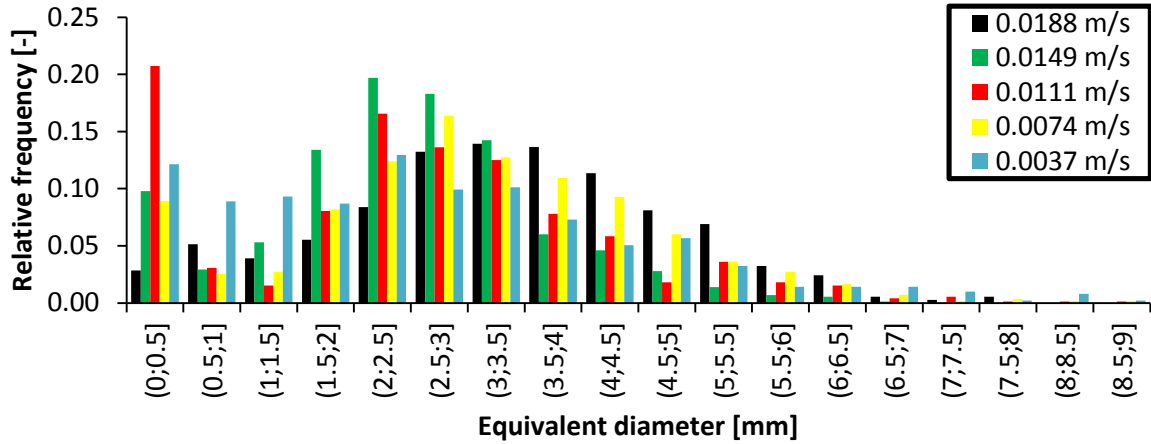


(a) Gas holdup curves

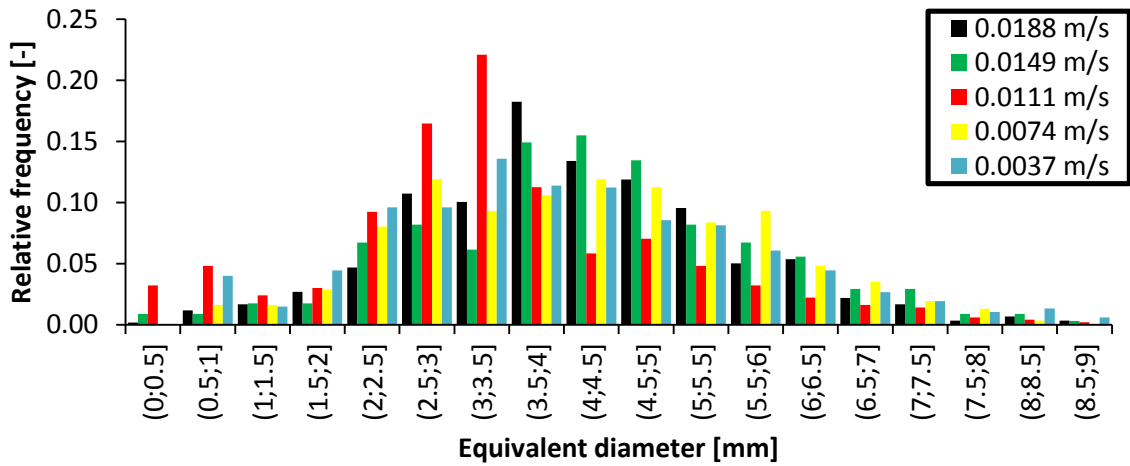
786 Figure 28 Gas holdup and flow regime transition (between the pseudo-homogenous flow  
787 regime and the transition flow regime) – Data from Besagni and Inzoli (2016a)

788

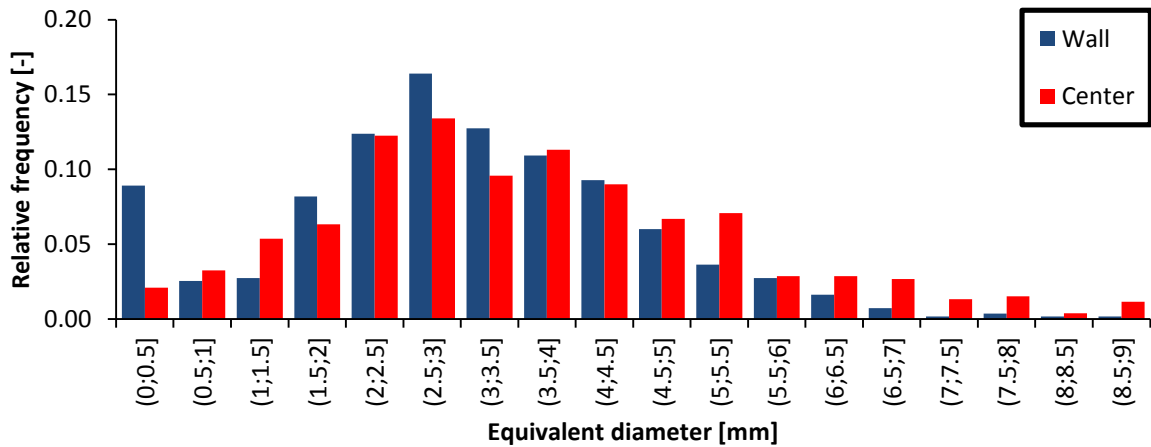
789



(a) Batch mode (measured at the center of the bubble column): influence of the superficial gas velocity

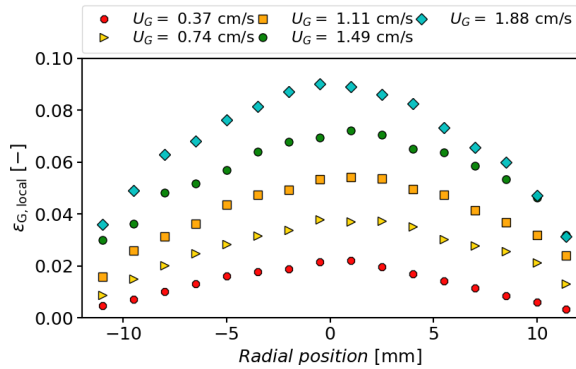


(a) Counter-current mode (measured at the center of the bubble column): influence of the superficial gas velocity.

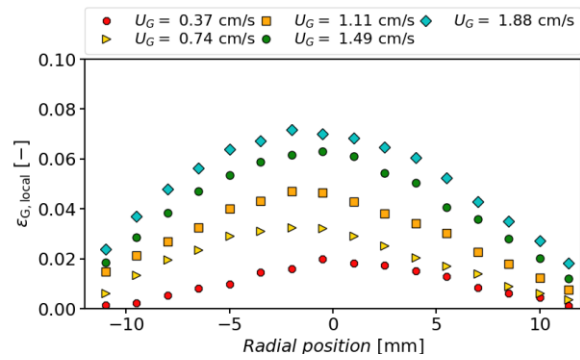


(a) Batch mode (at  $U_G = 0.37 \text{ cm/s}$ ): comparison between measurements at the center of the column and near the wall. – Data from Besagni and Inzoli (2016a)

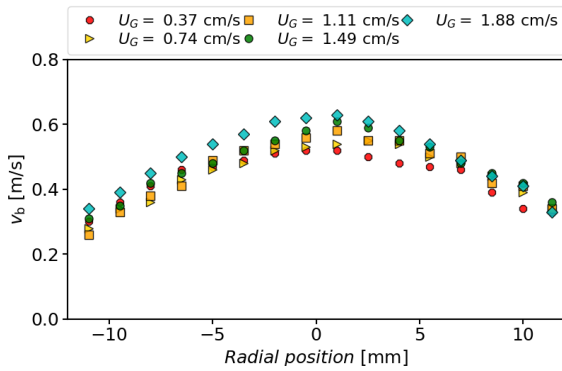
Figure 29 Bubble size distributions in the pseudo-homogeneous flow regime.



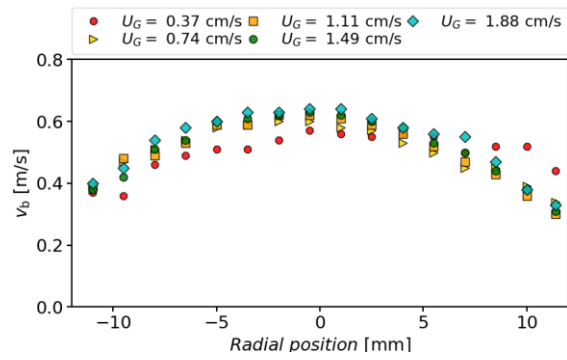
(a) void fraction profiles – 1.9 m above the gas sparger – batch mode



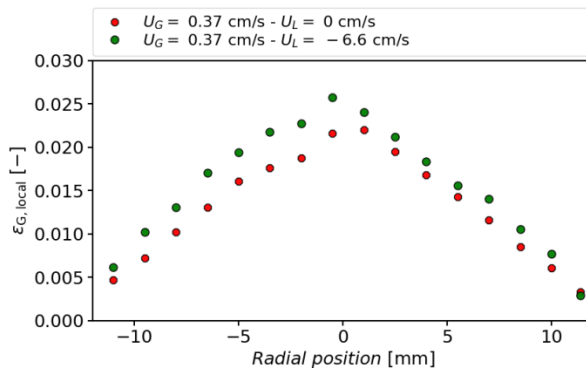
(b) void fraction profiles – 0.7 m above the gas sparger – batch mode



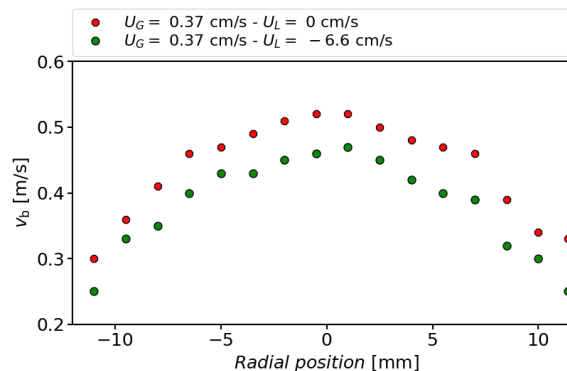
(c) bubble rising velocity – 1.9 m above the gas sparger – batch mode



(d) bubble rising velocity – 0.7 m above the gas sparger – batch mode



(e) void fraction profiles – 0.7 m above the gas sparger – influence of counter-current mode

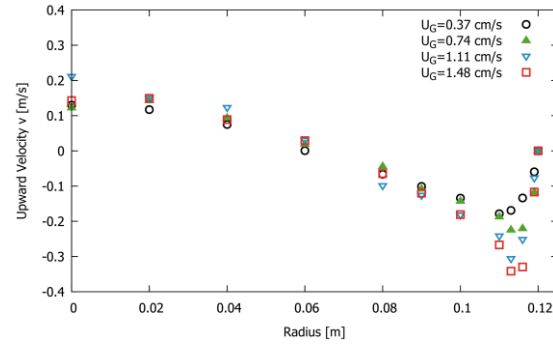
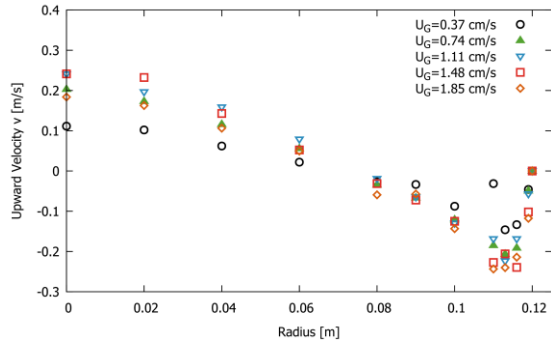


(f) bubble rising velocity – 1.9 m above the gas sparger – influence of counter-current mode

791 Figure 30 Local flow properties measured by the optical probe in the pseudo-homogenous  
 792 flow regime. – Data from Besagni and Inzoli (2016a)

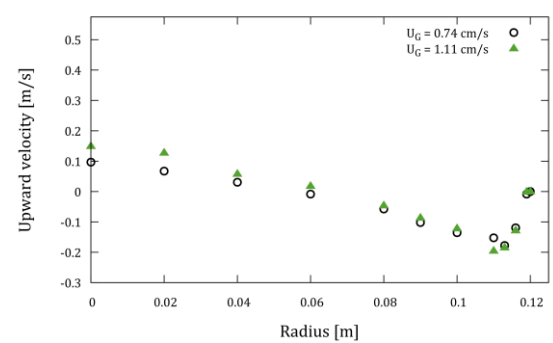
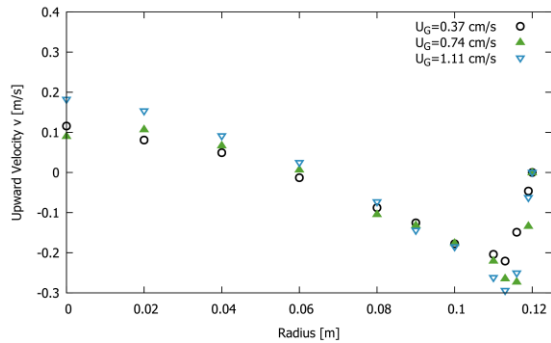
794 **B. Results 1.9 m above the sparger**

795 Since inlet effects are present at the measuring position 1.9 m above the sparger, these  
 796 results were not in the focus of the main text. For completeness, the results at this  
 797 measuring position are given in the following



a) Batch mode

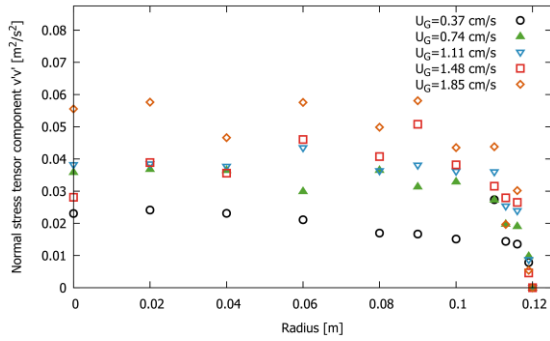
b) Superficial liquid velocity = -3.3 cm/s



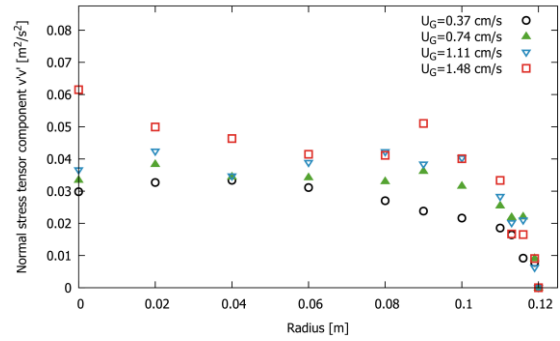
c) Superficial liquid velocity = -6.6 cm/s

d) Superficial liquid velocity = -9.2 cm/s

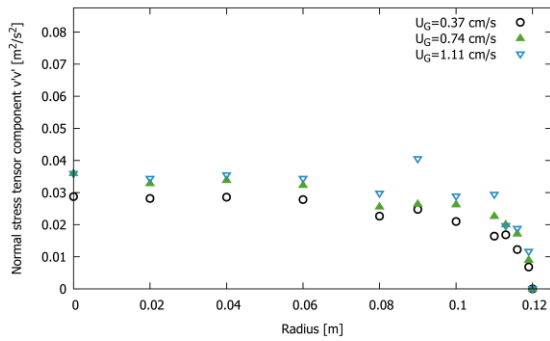
798 Figure 31 Averaged upward liquid velocities for different superficial gas velocities at  
 799 different superficial liquid velocities,  $U_L$ , 1.9 m above the gas sparger.



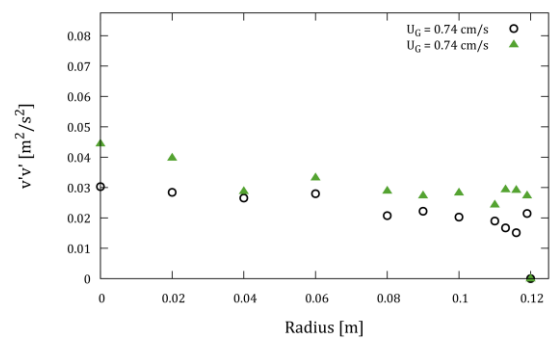
a) Batch mode



b) Superficial liquid velocity = -3.3 cm/s



c) Superficial liquid velocity = -6.6 cm/s



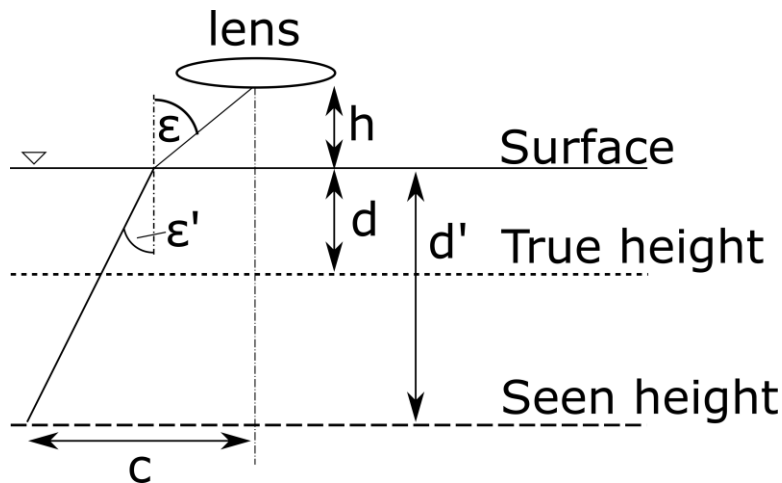
d) Superficial liquid velocity = -9.2 cm/s

800 Figure 32 Normal Reynolds stresses in upward direction for different superficial gas  
 801 velocities at different counter-current flow setups 0.7 m above the gas sparger.

802 C. Optical distortion

803 Due to the different Refraction indices, an optical distortion is present. This distortion is  
 804 in the following calculated based on the assumption made in Section 2.3 and as shown  
 805 in Figure 33.

806

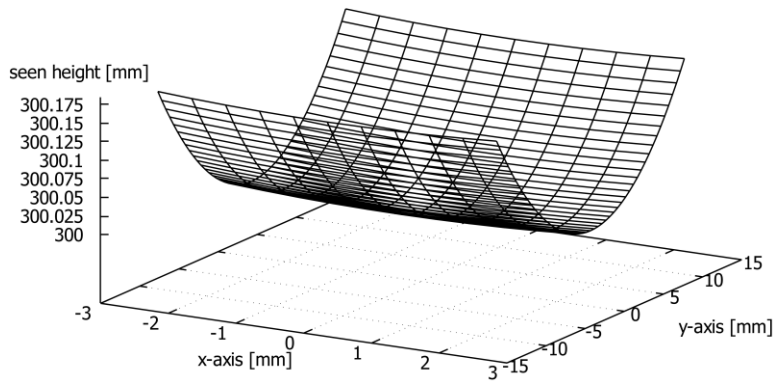


807

808

Figure 33 Calculating the distortion due to the different refracting indices.

809 Due to the different speed of light in water and Plexiglas, a light beam is refracted.  
810 Therefore, the depth of field is not a plane but rather a bend surface since the light  
811 refraction is a function of the distance to the surface,  $h$ , the distance from the lot,  $c$ , the focal  
812 length of the camera lens, and the water depth  $d$ . However, the effect of a bended depth of  
813 field is minor as shown in Figure 34, where the depth of field is shown for the measuring  
814 position in the center of the column. The deviation to a flat depth of field is below 0.175  
815 mm for all measuring positions; therefore, this effect can be neglected from now on.



816

817 Figure 34 Bended depth of field due to refraction in the present setup. At  $x = 0$  mm and  
818  $y = 0$  mm is the center of the picture.

## 819 7 References

- 820 Barnard, S. T. & Thompson, W. B., 1980. Disparity analysis of images. *IEEE Trans Pattern*  
821 *Analysis Machine Intelligence*, pp. 333-340.
- 822 Besagni, G., Inzoli, F., & Ziegenhein, T. 2018. Two-Phase Bubble Columns: A Comprehensive  
823 Review. *ChemEngineering*, 2(2), 13.
- 824 Besagni, G. et al., 2017. The effect of aspect ratio in counter-current gas-liquid bubble  
825 columns: Experimental results and gas holdup correlations. *International Journal of*  
826 *Multiphase Flow*, Volume 94, pp. 53-78.
- 827 Besagni, G. & Inzoli, F., 2016a. Comprehensive experimental investigation of counter-  
828 current bubble column hydrodynamics: Holdup, flow regime transition, bubble size  
829 distributions and local flow properties. *Chemical Engineering Science*, Volume 146, pp.  
830 259-290.
- 831 Besagni, G., & Inzoli, F. 2016b. Bubble size distributions and shapes in annular gap bubble  
832 column. *Experimental Thermal and Fluid Science*, 74, 27-48.
- 833 Bröder, D. & Sommerfeld, M., 2002. An advanced LIF-PLV system for analysing the  
834 hydrodynamics in a laboratory bubble column at higher void fractions. *Experiments in*  
835 *Fluids*, Volume 33, p. 826–837.
- 836 Bröder, D. & Sommerfeld, M., 2007. Planar shadow image velocimetry for the analysis of the  
837 hydrodynamics in bubbly flows. *Meas. Sci. Technol.*, Volume 18, p. 2513–2528.
- 838 Canny, J., 1986. A Computational Approach To Edge Detection. *IEEE Trans. Pattern Analysis*  
839 *and Machine Intelligence*, 8(6), p. 679–698.
- 840 Deen, N. G., Westerweel, J. & Delnoij, E., 2002. Two-Phase PIV in Bubbly Flows: Status and  
841 Trends. *Chem. Eng. Technol.* , Volume 25.
- 842 Delnoij, E., Kuipers, J. A. M., van Swaaij, W. P. M. & Westerweel, J., 2000. Measurement of  
843 gas-liquid two-phase flow in bubble columns using ensemble correlation PIV. *Chemical*  
844 *Engineering Science* , Volume 55, pp. 3385 - 3395.
- 845 Delnoij, E. et al., 1999. Ensemble correlation PIV applied to bubble plumes rising in a  
846 bubble column. *Chemical Engineering Science*, Volume 54, pp. 5159-5171.
- 847 Hessenkemper, H. & Ziegenhein, T., 2018. Particle Shadow Velocimetry (PSV) in bubbly  
848 flows. *Int. J. Multiph. Flow*, Accepted.
- 849 Hosokawa, S. & Tomiyama, A., 2013. Bubble-induced pseudo turbulence in laminar pipe  
850 flows. *Int. J. Heat Fluid Flow*, Volume 40, pp. 97-105.
- 851 Jakobsen, M. L., Easson, W. J., Greated, C. A. & Glass, D. H., 1996. Particle image velocimetry:  
852 simultaneous two-phase flow measurements. *Meas. Sci. Technol.* , Volume 7, p. 1270–1280.

853 Julia, J. E., Hernandez, L., Chiva, S. & Vela, A., 2007. Hydrodynamic characterization of a  
854 needle sparger rectangular bubble column: Homogeneous flow, static bubble plume and  
855 oscillating bubble plume. *Chemical Engineering Science*, 62(22), pp. 6361-6377.

856 Kitscha, J., & Kocamustafaogullari, G. 1989. Breakup criteria for fluid particles. *International*  
857 *Journal of Multiphase Flow*, 15(4), 573-588.

858 Lance, M. & Bataille, J., 1991. Turbulence in the liquid phase of a uniform bubbly air–water  
859 flow. *Journal of Fluid Mechanics*, Volume 222, pp. 95-188.

860 Lindken, R. & Merzkirch, W., 2002. A novel PIV technique for measurements in multiphase  
861 flows and its application to two-phase bubbly flows. *Experiments in Fluids*, Volume 33, pp.  
862 814-825.

863 Lopez de Bertodano, M. L., Lee, S. J. & Lahey, R. T., 1996. Quantitative analysis and  
864 computation of two-dimensional bubble columns. *A.I.Ch.E. Journal* , Volume 42, pp. 301-  
865 308.

866 Lucas, D. et al., 2016. A strategy for the qualification of multi-fluid approaches for nuclear  
867 reactor safety. *Nuclear Engineering and Design*, Volume 299, pp. 2-11.

868 D. Lucas, H.-M. Prasser and A. Manera, "Influence of the lift force on the stability of a bubble  
869 column," *Chemical Engineering Science*, vol. 60, p. 3609 – 3619, 2005.

870 Ma, T. et al., 2017. Direct numerical simulation–based Reynolds-averaged closure for  
871 bubble-induced turbulence. *Physical Review Fluids*, 2(3), p. 034301.

872 Mercado, J. M. et al., 2012. Lagrangian statistics of light particles in turbulence. *Physics of*  
873 *Fluids (1994-present)*, 24(5).

874 Mudde, R. F., Harteveld, W. F. & Van Den Akker, H. E. A., 2009. Uniform Flow in Bubble  
875 Columns. *Ind. Eng. Chem. Res.*, Issue 48, p. 148.

876 Murgan, I., Bunea, F. & Ciocan, G. D., 2017. Experimental PIV and LIF characterization of a  
877 bubble column flow. *Flow Measurement and Instrumentation*, Volume 54, pp. 224-235.

878 Nigmatulin, R. I., 1979. Spatial averaging in the mechanics of heterogeneous and dispersed  
879 systems. *Journal of Multiphase Flow*, Volume 5, pp. 353-385.

880 Ohmi, K. & Li, H.-Y., 2000. Particle-tracking velocimetry with new algorithms. *Meas. Sci.*  
881 *Technol.*, Volume 11, pp. 603-616.

882 Pang, M. & Wei, J., 2013. Experimental investigation on the turbulence channel flow laden  
883 with small bubbles by PIV. *Chemical Engineering Science*, Volume 94, pp. 302-315.

884 Reily, I. G., Scott, D. S., Debrujin, T. & Macintyre, D., 1994. The Role of Gas Momentum in  
885 Determining Gas Holdup and Hydrodynamic Flow Regimes in Bubble Columns. *The*  
886 *Canadian Journal of Chemical Engineering*, Volume 1, p. 72.

887 Rensen, J., Luther, S., de Vries, J. & Lohse, D., 2005. Hot-film anemometry in bubbly flow I:  
888 bubble–probe interaction. *International Journal of Multiphase Flow*, 31(3), pp. 285-301.

889 Rzehak, R., Krauß, M., Kováts, P. & Zähringer, K., 2017. Fluid dynamics in a bubble column:  
890 New experiments and simulations. *International Journal of Multiphase Flow*, Volume 89,  
891 pp. 299-312.

892 Sasaki, S., Hayashi, K., & Tomiyama, A. 2016. Effects of liquid height on gas holdup in air–  
893 water bubble column. *Experimental Thermal and Fluid Science*, 72, 67-74.

894 Sasaki, S., Uchida, K., Hayashi, K., & Tomiyama, A. 2017. Effects of column diameter and  
895 liquid height on gas holdup in air-water bubble columns. *Experimental Thermal and Fluid*  
896 *Science*, 82, 359-366.

897 Schleicher, E., Da Silva, M. & Hampel, U., 2008. Enhanced Local Volume and Temperature  
898 Measurements for Highly Transient Multiphase Flows. *Instrumentation and Measurement*,  
899 *IEEE Transactions on*, Feb, 57(2), pp. 401-405.

900 Shaikh, A., & Al-Dahhan, M. 2013. Scale-up of bubble column reactors: a review of current  
901 state-of-the-art. *Industrial & Engineering Chemistry Research*, 52(24), 8091-8108.

902 Tomiyama, A., 2002. Single Bubbles in Stagnant Liquids and in Linear Shear Flows.  
903 Dresden, Germany, Workshop on Measurement Technology (MTWS5).

904 Trivedi, R., Renganathan, T., & Krishnaiah, K. 2018. Hydrodynamics of countercurrent  
905 bubble column: Experiments and predictions. *Chemical Engineering Journal*, 338, 636-650.

906 Ueyama, K., & Miyauchi, T. 1979. Properties of recirculating turbulent two phase flow in gas  
907 bubble columns. *AIChE Journal*, 25(2), 258-266.

908 Ziegenhein, T., Garcon, M. & Lucas, D., 2016a. Particle tracking using micro bubbles in  
909 bubbly flows. *Chem. Eng. Sci.*, Volume 153, pp. 155-164.

910 Ziegenhein, T. & Lucas, D., 2016b. On sampling bias in multiphase flows: Particle image  
911 velocimetry in bubbly flows. *Flow Measurement and Instrumentation*, Volume 48, pp. 36-  
912 41.

913 Ziegenhein, T., Zalucky, J., Rzehak, R. & Lucas, D., 2016c. On the hydrodynamics of airlift  
914 reactors, Part I: Experiments. *Chemical Engineering Science*, Volume 150, pp. 54-65.

915 Wilkinson, P. M., Spek, A. P., & van Dierendonck, L. L. 1992. Design parameters estimation  
916 for scale-up of high-pressure bubble columns. *AIChE Journal*, 38(4), 544-554.

917